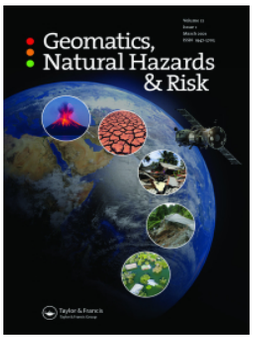

Geomatics, Natural Hazards and Risk

ISSN: (Print) (Online) Journal homepage: www.tandfonline.com/journals/tgnh20

Synergistic use of SAR satellites with deep learning model interpolation for investigating of active landslides in Cuenca, Ecuador

Mohammad Amin Khalili, Silvio Coda, Domenico Calcaterra & Diego Di Martire

To cite this article: Mohammad Amin Khalili, Silvio Coda, Domenico Calcaterra & Diego Di Martire (2024) Synergistic use of SAR satellites with deep learning model interpolation for investigating of active landslides in Cuenca, Ecuador, Geomatics, Natural Hazards and Risk, 15:1, 2383270, DOI: 10.1080/19475705.2024.2383270

To link to this article: https://doi.org/10.1080/19475705.2024.2383270

GEOMATICS, NATURAL HAZARDS AND RISK
2024, VOL. 15, NO. 1, 2383270
https://doi.org/10.1080/19475705.2024.2383270

Taylor & Francis
Taylor & Francis Group

Synergistic use of SAR satellites with deep learning model interpolation for investigating of active landslides in Cuenca, Ecuador

Mohammad Amin Khalili, Silvio Coda, Domenico Calcaterra and Diego Di Martire

Department of Earth, Environmental and Resource Sciences, Federico II University of Naples, Naples, Italy

ABSTRACT

Among the most intense geological disasters, landslides frequently occur throughout the world. These phenomena have been studied using space geodetic techniques, including Global Navigation Satellite Systems (GNSS) and Multi-Temporal Interferometric Synthetic Aperture Radars (MT-InSAR). Nevertheless, complete mapping and analysis of landslides' surface deformation in most areas can be complicated due to a large diversity in kinematics, such as periods of quiescence and acceleration in the toe and crown. One of these landslides is the Cuenca landslides in Ecuador, where the geological investigation revealed that the toe of the landslides was located in urban areas, with more noticeable deformation effects. In contrast, its crown was located mainly in a rural and green land area. In this study, we show the potential of a synergistic use of COSMO-SkyMed (CSK) and Sentinel-1A (S1A) synthetic aperture radar (SAR) data for comprehensively monitoring the Cuenca landslides. To this aim, we have used Long-Short Term Memory (LSTM) and Convolutional Neural Networks (CNN) as two different Deep Learning Algorithms (DLAs) to integrate results in the temporal and spatial domain, respectively. A cross-comparison of the results was made with the nine GPS-derived deformations and the visual effects (i.e. crack width and pattern) on the field. This validation against GPS observation reveals that the RMSEs of the final MT-InSAR-derived velocity after applying the synergic double band SAR dataset decrease at more than 73% of nine GPS stations.

HIGHLIGHTS

- Synergic MT-InSAR approach for studying landslide deformation in diverse kinematic areas.
- Utilized DLAs (LSTM and CNNs) for effective temporal and spatial interpolation of InSAR results.
- Findings emphasize the potential of multi-sensor SAR and DLAs for landslide monitoring regarding improving the RMSE at nine stations with an average of 73%.

ARTICLE HISTORY

Received 14 November 2023
Accepted 18 July 2024

KEYWORDS

Landslide; MT-InSAR; Convolutional Neural Networks (CNN); Long-Short Term Memory (LSTM); Cuenca

CONTACT Mohammad Amin Khalili mohammadamin.khalili@unina.it

GRAPHICAL ABSTRACT

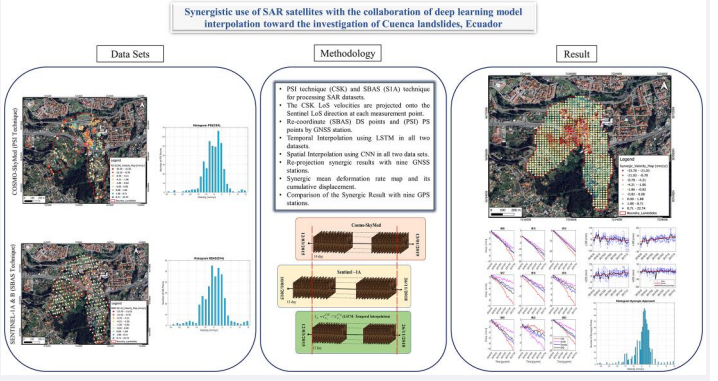

1. Introduction

Rural and urban areas are vulnerable to landslides, constituting a significant geological hazard (Rianna et al. 2023). In rural areas, landslides can severely impact agricultural operations and even result in loss of life (Solari et al. 2020; Zhao et al. 2021). In addition, in urban environments, landslides can cause extensive damage to residential and commercial structures, disrupt public utilities, and compromise road networks (Esmaeeli et al. 2023; Khalili et al. 2023; Pu et al. 2023). The study of landslides kinematics (i.e. the description of motion without considering the forces that cause it) is critical to mitigating their destructive effects (Amin Khalili et al. 2024). The factors influencing landslides kinematics may include the stability of slopes, patterns of precipitation (Shi et al. 2022), the type of soil, and the extent of vegetation cover (Guzzetti et al. 2012). Also, human activities such as urban development, construction practices, and alteration of natural landscapes add complexity to the kinematics of landslides in these contexts (Guerriero et al. 2019; Das et al. 2020). Therefore, understanding landslides kinematics is crucial for developing effective strategies for disaster preparedness and risk reduction in both rural and urban areas (Khalili et al. 2024).

GNSS and remote sensing SAR interferometry have been used as essential tools for studying the kinematics of landslides in rural and urban settings (Zhao and Lu 2018; Del Soldato et al. 2021; Khalili et al. 2023; Sonnessa et al. 2023). Interferometry SAR has been developed for decades in various ways that have improved precision and accuracy (Kumar et al. 2011; Mullissa et al. 2017). In brief, Interferometric Synthetic Aperture Radars (InSAR) is a type of two-SAR image processing technique (Gabriel et al. 1989), while Multi-Temporal InSAR (MT-InSAR) is a multi-SAR image time series processing technique (Franceschetti and Lanari 1999). To improve the implementation of the MT-InSAR method, different concepts have emerged in recent years, such as Smal BAseline Subset (SBAS) (Berardino et al. 2002; Lanari et al. 2004) and Permanent Scatterers Interferometry (PSI) (Ferretti et al. 2001; Hooper et al. 2004). Each has its benefits and drawbacks when retrieving spatio- and temporal aspects of

surface deformations over short and long periods in different types of locations (Babaee et al. 2024; Tasan et al. 2024).

Previous research in the area of interest (Cuenca-Ecuador) has utilized similar technologies, advancing our understanding of landslide dynamics. Notable works include Khalili et al. (2023), who assessed MT-InSAR processing techniques for landslide monitoring, and Di Napoli et al. (2023), who performed a multitemporal relative landslide exposure and risk analysis. Additionally, Sellers et al. (2021) monitored ground deformation affecting strategic buildings, while Miele et al. (2021) developed a Landslide Awareness System to enhance the resilience and safety of transport infrastructure, particularly along the Pan-American Highway.

The SBAS method uses interferograms network with minimal temporal and spatial baselines for assessing land deformations. This method is particularly adept at utilizing distributed scatterers (DSs) (i.e. radar reflectors that exhibit smooth variations over a specific period of time). DS pixels are primarily found in agricultural areas or natural terrains (green areas), which enhances the efficacy of the SBAS method for studying deformations in this area (Berardino et al. 2002). While the PSI method uses Permanent Scatterers (PSs) (i.e. radar reflectors that exhibit temporal phase stability over time) to measure deformation (Hanssen and Ferretti 2002) that are mostly found in urban areas. Therefore, unlike the SBAS method, this method is less efficient in green areas due to the unavailability of stable scatterers (Delgado Blasco et al. 2019).

In addition, the C-band SAR images operate at a lower frequency, enabling a greater signal penetration depth into the ground surface (Li et al. 2023). This attribute is particularly advantageous in vegetated areas where the signal can penetrate foliage to detect ground movements, a task where X-band SAR images encounter difficulties due to their limited penetration depth. However, the lower frequency C-band comes with a lower spatial resolution compared to the X-band. Consequently, its effectiveness in delineating fine-scale features and individual structures is compromised, potentially limiting the accuracy of defining landslide boundaries. The X-band provides superior spatial resolution, allowing it to analyze landslide boundaries and detect smaller deformations in detail (Chini et al. 2015; Tings et al. 2021; Bausilio et al. 2024).

The unique advantages of both C-band and X-band and those of PSI and SBAS techniques highlight the necessity of a synergistic approach in landslide studies. The joint use of double-band SAR imagery can exploit the higher spatial resolution and sensitivity to small deformations of the X-band, compensating for the reduced coverage and penetration of the C-band, especially in densely green areas. Furthermore, the synergy between PSI and SBAS allows for a more detailed understanding by combining their results as complementary to each other, mainly due to high PS and DS density in urban and non-urban areas, respectively (Bonano et al. 2013; Nunziata et al. 2016). Therefore, the simultaneous application of both double-band SAR imagery and multiple techniques enables a more nuanced understanding of landslide kinematics and boundaries, optimizing each method's strengths and mitigating their weaknesses. Therefore, to fully map and analyze landslides' surface deformation and its kinematics in urban and rural areas, one may need to combine the abovementioned concepts as a synergic approach (Busquier et al. 2022).

In this regard, several studies have focused on multi-sensor data fusion (Samsonov and d'Oreye 2012; Lin et al. 2016; Pepe et al. 2016; Sun et al. 2016; Chen et al. 2021; Jiang et al. 2023). These methods are either often used to combine time series in the temporal domine or exploit the limitations of the model and do not fully consider the nature of the observations. However, the spatiotemporal multi-sensor data fusion might be influenced by various factors and often show difference characteristics. In this article, synergistic fusion of PSI and SBAS results based on spatiotemporal deep learning method allows us to leverage the strengths of both methods and explores intricate relationships between different observations. In addition, it is worth noting that two InSAR datasets (Sentinel-1 and CSK) used in this study have different wavelengths (i.e. C-band and X-band), which allow us to apply these data to monitor different regions based on the required monitoring accuracy.

Therefore, we employed a deep learning model for spatial and temporal interpolation to execute this synergic approach. Long Short-Term Memory (LSTM) models are utilized for temporal interpolation due to their remarkable capacity to learn long-term dependencies in time series data, allowing for robust reconstruction of missing time steps in a new timeframe (Suzuki and Ikehara 2020; Liu et al. 2022; Khalili et al. 2023). Convolutional Neural Networks (CNNs) are the preferred choice for spatial interpolation in this study (Otake et al. 2020; Dong et al. 2021). Its ability to extract spatial features and learn complex patterns from data makes it well-suited for predicting unobserved data points in space, ensuring the continuity and spatial integrity of the resultant grid. Thus, using LSTM and CNN for temporal and spatial interpolation, respectively, can significantly enhance the quality and coherence of the final data representation, promoting a more reliable and insightful landslide analysis (Mu et al. 2023).

In conclusion, our approach is leveraging CNN and LSTM for interpolation purposes. Our methodology seeks to bridge the gap in traditional remote sensing techniques by introducing a synergic approach combining CSK and S1A by CNN and LSTM to yield more accurate and interpretable velocity and time series maps. This approach not only provides enhanced detail of landslide monitoring but also paves the way for better risk assessment, kinematic analysis, and mitigation planning for areas prone to landslides. The article's findings led us to adopt the suggested methodology, aiming to enhance the visibility of unstable areas using a synergistic approach with specific SAR bands (i.e. C and X).

2. Case study and geological setting

The area is located in the south-eastern Cuenca city's sector with an extension of about 3 km^2. The University of Azuay's main campus is centrally located and is crossed by the Pan-American Highway from west to east (Figure 1a).

The area falls into the Cuenca basin in the Inter-Andean region (Litherland 1994), and from south-east to north-west, the Miocene terrigenous formations of Azogues (tuffaceous sandstones), Mangan (siltstones and conglomeratic sandstones), and Turi (coarse conglomerates) crop out (Figure 1a) (Hungerbühler et al. 2002). These formations are characterized by substantial heterogeneity in stratigraphy and mechanical

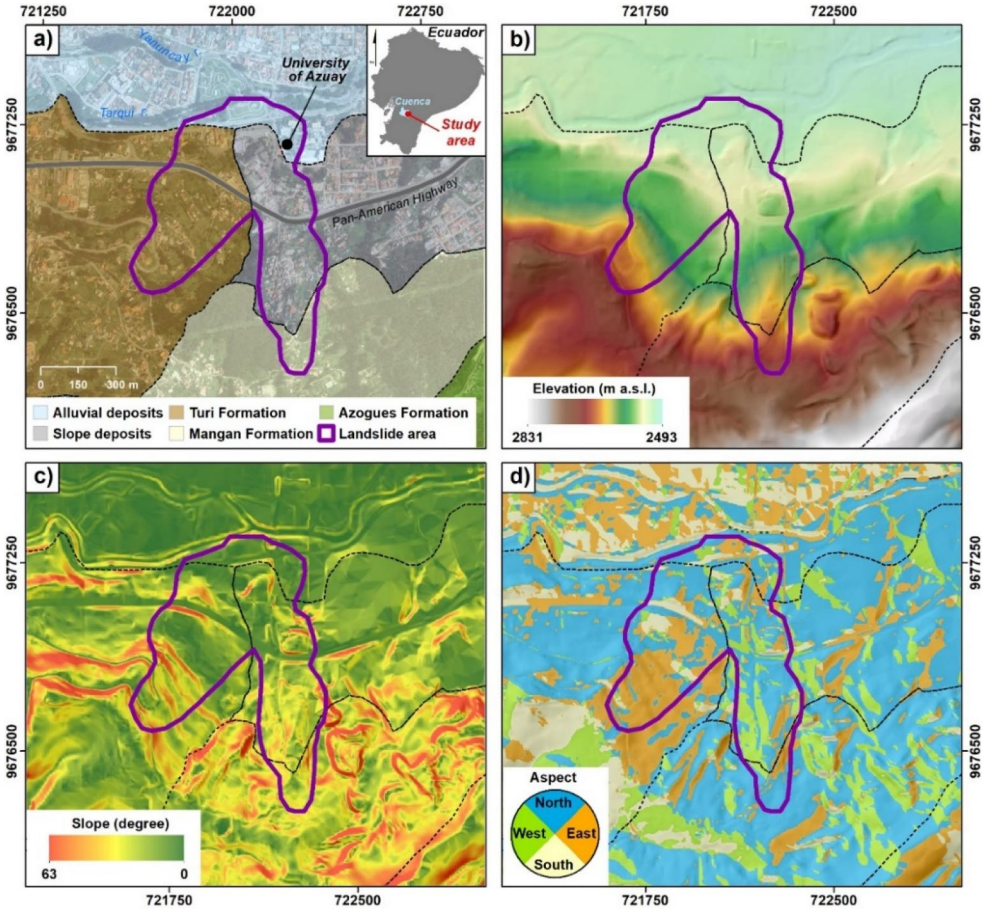

Figure 1. Geological sketch map (a), DTM (b), slope (c), and aspect (d) of the study area.

properties due to different sediments' origins (fluvial, alluvial, colluvial, and volcanic), which leads to different susceptibility to trigger landslides. The study area's eastern and northern sectors are covered by quaternary deposits, specifically colluvial and alluvial deposits, respectively (Hungerbühler et al. 2002; Miele et al. 2021).

The highest elevation values are recorded in the southern sector, up to 2830 m a.s.l. (Figure 1b), where the steepest slopes are also present up to values of 60 degrees (Figure 1c), thanks to the outcropping of materials that are more lithoid and, therefore, capable of giving rise to sub-vertical slopes (Turi Formation). On the contrary, the eastern slope, where both the upper sector, falling within the Mangan formation, and the central sector (slope deposits) show medium slopes (approximately), while the lower sector records rather limited acclivities, being in the foothill sector. Regarding the morphological aspect, two main sectors can be distinguished, east-facing slopes in the westernmost sector and north-west-facing slopes in the easternmost sector (Figure 1d). This morphology suggests the presence of two different basins which are channelled into the main impluvium that passes underneath the structures of the University campus. In fact, the morphology highlights the presence of a hydrographic network with the Tomebamba stream as its destination.

The landslides surveyed since 1997 are represented by rotational slides and falls, causing damaging effects on buildings and linear infrastructures, as reported by several recent studies (Sellers et al. 2021). Several rupture surfaces were detected by geotechnical surveys, up to 80 m of depth, estimating an approximate volume of more than 35 million m^3 (Ammirati et al. 2020; Sellers et al. 2021). Unfortunately, geognostic investigations or even sampling to define the physical-mechanical characteristics of the materials involved have never been carried out. The only investigations carried out are of the geophysical type (Electrical Tomography and Seismic Refraction and Reflection) which have allowed, in certain areas, to define a probable flow surface at a depth of about 17 m (Sellers et al. 2021). The test area for the developed methodology (see purple polygon in Figure 1) has an extension of approximately 0.44 km^2 and involves two slope sectors facing east and northwest, respectively.

3. Data sets

This manuscript utilizes several rich datasets to comprehensively study land deformation, explicitly focusing on landslides in urban and rural areas. The first dataset comes from the S1A missions, courtesy of the European Space Agency (ESA) (Bonnet and Manno 1994). These missions operate in the C-band. The S1A dataset is composed of images captured over several years. Specifically, the study utilized an ascending S1A radar images track acquired between 10 January 2015 and 26 November 2018, consisting of 61 Single Look Complex (SLC) images (Table 1).

The second dataset leverages the capabilities of the CSK constellation (F. Covello et al. 2010). CSK, funded by the Italian Space Agency (ASI), is a constellation of four medium-sized low-Earth orbit satellites (Bovenga et al. 2010). These satellites are equipped with high-resolution multi-mode SAR sensors that operate in the X-band. The dataset from CSK, consisting of 57 SLC SAR images collected over an ascending geometry track between 12 March 2015 and 13 January 2019, is used (Table 1). Each image covers a $40 \times 40\,km^2$ area, providing substantial spatial coverage and further enhancing the data quality available for the study.

The third data set includes data from GPS stations around the area of study (i.e. consisting of eleven permanent stations) (Figure 4). In the context of this study, GPS stations facilitate spatial coordination and adjustment of the deformation measurements derived from the SAR images (stations including M21, and M01). They also serve a validation role, confirming the outcomes derived from the synergic SAR images in X- and C-bands.

Table 1. Specifications of the S1A and CSK acquisitions.

Information	S1A	CSK
Acquisition time	January 10, 2015, November 26, 2018	March 12, 2015, January 13, 2019
Type	SLC	SLC
Images (Nr)	61	57
Swath	IW2	–
Pass	Ascending	Ascending
Central Look Angle (°)	34	29
Polarization	VV	HH

Note that the L-band SAR images offering deeper penetration capabilities, especially in vegetated areas, can also introduce issues related to volumetric scattering in regions with dense vegetation. Additionally, the availability of L-band data was limited for the specific regions under investigation in our study. Given our focus on the University of Azuay and the Pan-American highway regions, encompassing urban and rural-green areas, the C- and X-bands provided the requisite spatial resolution and minimized scattering effects in urban settings. Also, the combination of S1A and CSK images in C- and X-bands, respectively, offered the optimal balance of penetration depth and resolution for our specific objectives.

4. Methodology

4.1. SAR data processing

SAR data analysis forms the core of this study, employing both PSI and SBAS approaches. We applied the PSI technique to analyze CSK images within the SUBSOFT package (Mora et al. 2003; Iglesias et al. 2015). The Coherent Pixels Technique - Temporal Phase Coherence (CPT-TPC) was used to process the data during this phase. This technique is instrumental in identifying all possible interferogram pairs with perpendicular and temporal baselines concerning a single master image, which are 400 m and 100 days, respectively.

The decision to employ the PSI technique for processing CSK images derives from the inherent characteristics and advantages of both the imaging system and the method itself. CSK, with its high-resolution capabilities, offers a dense network of PSs in urban areas, which are particularly suited for PSI analysis. PSI excels in environments with many stable scatterers, like those found in urban settings, allowing for precise deformation monitoring over extended periods.

A Temporal Phase Coherence (TPC) threshold of 0.7 was set to ensure high-quality data. Only those points that exceeded this threshold were considered for more advanced analyses. Implementing this selective method ensured that the outputs, including the Line of Side (LoS) deformation rate map and time series, offered a high-precision view of the deformation. The PSI technique used a 10×10 m Digital Elevation Model (DEM). Also, the 3×3 multi-looking factor was applied in both range and azimuth.

We applied the SBAS technique using the InSAR Scientific Computing Environment (ISCE) (Rosen et al. 2011; Agram et al. 2016) and MintPy (Yunjun et al. 2019) packages. During the processing of the S1A images, the SNAPHU phase unwrapping algorithm (Chen and Zebker 2001), with a threshold of 0.05 selected to limit noise and ensure high-quality interferograms, was utilized. The perpendicular baseline was fixed at 100 m for S1A images, with a temporal baseline of 90 days. These parameters were carefully chosen to facilitate the detection of deformation patterns across varying spatial and temporal scales. The SBAS technique was implemented using a DEM with a cell resolution of 30×30 m and multi-looking with a factor of 3×9 to enhance the coherence and reduce noise. In total, 234 interferogram pairs were generated for the S1A dataset.

SBAS is particularly adept at analyzing datasets with more DS points, such as those presented in S1A's coverage in rural and green areas. While it might seem straightforward to process both datasets with SBAS, using PSI for CSK allows us to exploit the strengths of each method and dataset combination, ensuring optimal results and a comprehensive understanding of the landslides phenomena across varied terrains and resolutions.

4.2. Synergic of SAR processed results

Using CSK, PS points, and S1A, DS points synergistically leverage the strengths of both satellites. Our data integration approach is outlined in the following four steps:

1. Unification of the measurement geometries in observation points, i.e. projecting LoS velocities in the CSK dataset into the direction of S1A LoS velocities.
2. Equalization of the measurement time epochs in the time series of each point in different datasets, i.e. performing a temporal interpolation with the LSTM model (Figure 5).
3. The spatial datum of different datasets is equalized using the existing GPS stations in the region, chosen as reference geometry.
4. Construct a unique spatial dataset based on interpolating different datasets on a regular grid (after hyperparameter tuning by the CNN model), i.e. two datasets have been joined and interpolated using the CNN model.

The following details of each of these steps are explained, and the overview flowchart of the synergic approach is designed below (Figure 2).

To ensure the reproducibility of our study and to facilitate similar investigations in high-altitude regions prone to landslides, we utilized a combination of various software tools and libraries for the implementation of our temporal and spatial interpolation methods. The LSTM and CNN models for temporal and spatial interpolations were developed using Python, leveraging libraries such as TensorFlow and Keras for deep learning, Pandas for data manipulation, and NumPy for numerical operations. Additionally, for geospatial analysis and visualization, we used QGIS 3.22 and ArcGIS 10.8, which provided robust tools for managing and analyzing spatial data. These platforms enabled the integration of various datasets and facilitated the creation of detailed maps. MATLAB 2022a was employed for further statistical analysis and validation, particularly in refining the interpolation results and ensuring their accuracy against ground truth data.

4.2.1. Projection with local incident angle

When integrating different datasets, it is crucial to consider the imaging geometry of the sensor, specifically factors like the imaging track and the incidence angle. Given that both datasets have an ascending geometry, the primary differentiation lies in the incidence angle of data collection. Multiple-satellite LoS velocities are given in the native incidence angles of both datasets. CSK satellite images at an average angle of 30 degrees, whereas the S1A images at about 43 degrees. To effectively merge the LoS

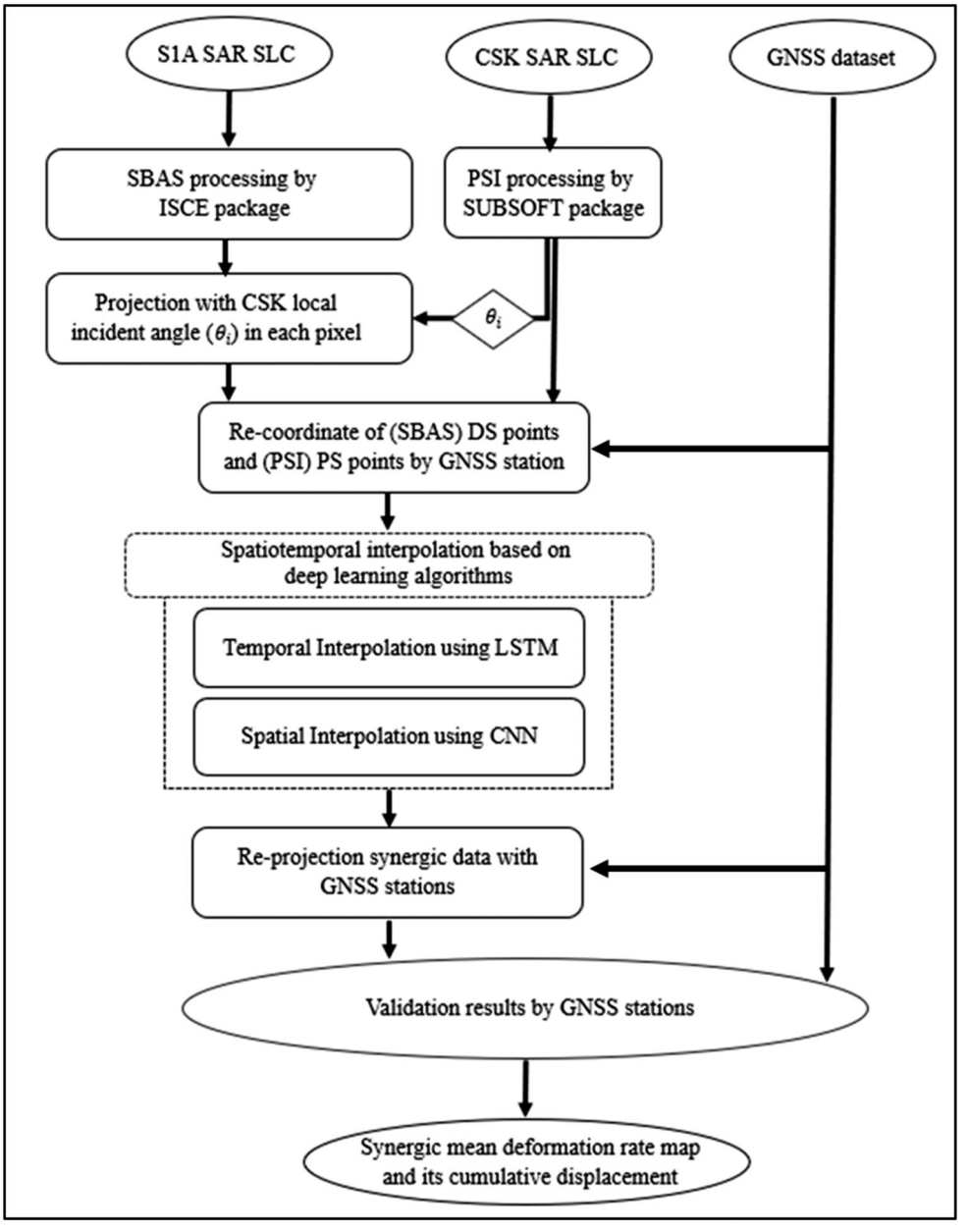

Figure 2. The flowchart of the synergic approach.

velocities, they must first be aligned to a shared incidence angle. This is done by computing the difference in incidence angles for each pixel between the CSK and S1A datasets. The CSK LoS velocities are then projected onto the S1A LoS direction at each measurement point as:

$$V_{\mathrm{CSK}}^{\mathrm{Proj}} = \frac{V_{\mathrm{CSK}}}{cos(\alpha_1 - \alpha_2\ )} \tag{1}$$

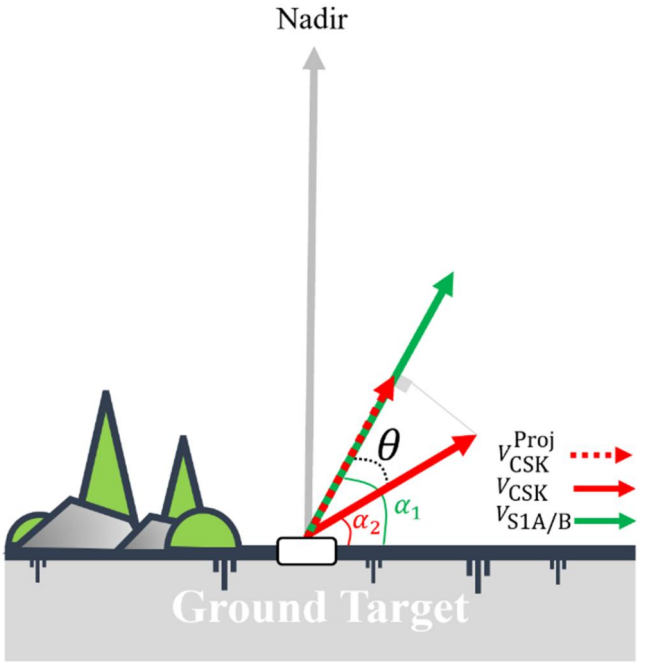

Figure 3. Schematic of multiple-satellite LoS-velocities geometry.

$V_{\mathrm{CSK}}^{\mathrm{Proj}}$ is a projected velocity on Sentinel LoS, V_{CSK} is CSK-derived LoS velocity, α_1 and α_2 are local incidence angles in Sentinel and CSK, respectively.

Figure 3 schematically depicts the geometry of the S1A incidence angle compared to the CSK incidence angle.

4.2.2. Re-coordinate of DS and PS points by GPS station

Because deformations in various datasets are based on different reference points, we use the regional GPS station (M21) as standard reference geometry to align the final interpolated deformation measurements. The light-blue triangles in Figure 4 are the location of the GPS stations. To carry out this re-coordination, firstly, the 3D deformation vectors of GPS are projected to the imaging geometry along the LoS of the satellite using the following relationship:

$$GNSS_{Los} = D_{up}\cos\theta + D_{ns}\sin\theta\sin\alpha - D_{ew}\sin\theta\cos\alpha \tag{2}$$

Where θ represents the incidence angle and α the azimuth angle. D_{up}, D_{ns}, and D_{ew} denote the up-down, north-south, and east-west deformation components, respectively. The difference between the GPS station's time series and the MT-InSAR time series is then computed.

Note that in order to avoid the problem of retrieving the real 3D displacement field in this study, our analysis applied in both PS/SBAS measurements along the LoS geometry which have the vectoral nature, and therefore all the analysis is done on this basis. Interestingly, the specific direction of real displacement did not significantly impact the final results of our analysis.

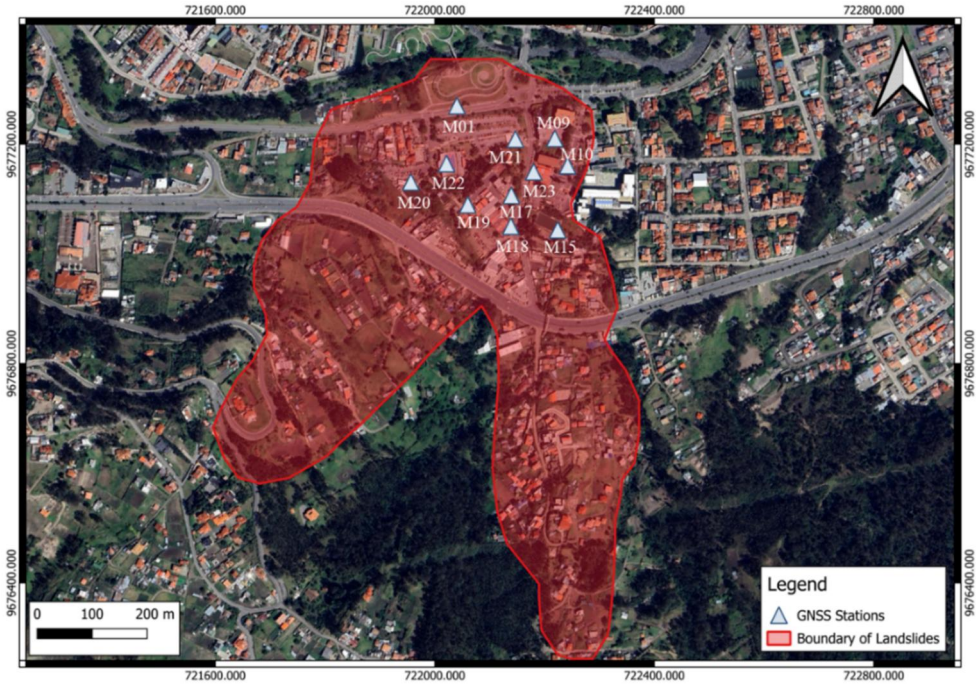

Figure 4. The location of eleven GPS stations (M01 and M21 used as reference points and others used for validation) in the study area.

4.2.3. Temporal and spatial interpolation

In addressing the temporal and spatial dimensions of landslide deformation analysis, this study leverages the advanced capabilities of LSTM and CNN algorithms. Unlike traditional interpolation methods, these deep learning algorithms excel in recognizing complex patterns and ensuring high precision in displacement measurements. The choice of LSTM is justified by its proficiency in capturing long-term dependencies within temporal sequences, a crucial aspect for understanding the dynamics of landslide movements. Similarly, CNN's effectiveness in spatial interpolation stems from its ability to preserve essential spatial features within displacement fields.

We utilized two distinct SAR datasets—CSK processed *via* the PSI technique and S1A processed with the SBAS method—to generate cumulative displacement data for a study area. Key steps include synchronizing the time intervals of the CSK and S1A datasets to a uniform 12-day cycle (mirroring the S1A acquisition frequency) with the same start and end date (obtained by the intersection of S1A and CSK acquisition time), followed by temporal interpolation of these datasets by LSTM algorithms. These interpolated datasets then serve as input for CNN algorithms to conduct spatial interpolation, culminating in generating a time series of displacements. This procedure ultimately yields a final velocity map *via* a synergic approach. To validate the accuracy and improvements achieved by this method, time series displacement data from nine GPS stations in the region are employed as ground truth references.

This uniform temporal spacing does not imply an alteration of the S1 dataset, which inherently aligns with the 12-day cadence, except in cases of missing

acquisitions (For example, the first date of acquisition, which is equivalent to 12/03/2015, is comparable to the first date of acquisition of CSA images.). Conversely, the CSK data are subjected to temporal interpolation to coincide with the S1 acquisition dates, facilitating a synchronized comparison. It is crucial to acknowledge the differential interpolation effect on the CSK dataset and its potential implications for interpolation accuracy. This distinction underscores the nuanced approach taken to merge these datasets while maintaining their integrity and the fidelity of their respective measurements.

While there are indeed many deep learning algorithms available, the selection should always be based on the nature of the data and its specific challenges. For InSAR interpolation, where we deal with complex temporal sequences and intricate spatial patterns, the combination of LSTM and CNN provides a robust and effective solution. Their combined use ensures a comprehensive capture of the intricate temporal trends and spatial patterns inherent in InSAR data, thus enabling a more accurate and detailed interpolation.

Temporal interpolation using LSTM: The first stage in our methodology concerns addressing temporal discrepancies among the datasets. This step is crucial to ensure we compare the same temporal time steps and intervals across all datasets. We used LSTM, a recurrent neural network apt for managing time series data.

Introduced by Hochreiter & Schmidhuber (Hochreiter and Schmidhuber 1996), LSTM is tailored to learn long-term dependencies and counters the vanishing gradient issue. It consists of a cell state and three gates (forget, input, and output). Each gate uses a sigmoid activation function, which confines the output between 0 and 1, optimizing gate operations.

The primary strength of LSTM lies in its ability to process sequential data. InSAR temporal data is sequential in nature, recording cumulative deformation over a series of time points. LSTM can remember patterns over long sequences and is less susceptible to the vanishing gradient problem, making it suitable for detecting trends or patterns over extended periods (Kong et al. 2018). LSTMs can adaptively learn the temporal dependencies of InSAR data. The gates in the LSTM units, such as the forget gate, input gate, and output gate, allow the network to learn and decide what information to store, update, or discard. This ensures that only relevant temporal features contributing to the deformation are considered (Monner and Reggia 2012). Unlike many other algorithms, LSTMs can generalize patterns across different time scales. This property is beneficial when dealing with InSAR data with deformations occurring at varied intervals based on the CSK and S1A timesteps. LSTM gates information and equations can be found in Liu et al. (2022).

This study addresses the challenge of integrating S1A and CSK datasets, characterized by differing acquisition frequencies, into a unified analysis framework. By employing the LSTM algorithm, we bridged the temporal gaps between these datasets, standardizing the measurement intervals to a consistent twelve-day cycle, reflective of S1A's operational frequency. As depicted in Figure 5, this temporal harmonization leverages LSTM's capabilities in time series prediction to align CSK's cumulative deformation measurements with S1A's temporal grid.

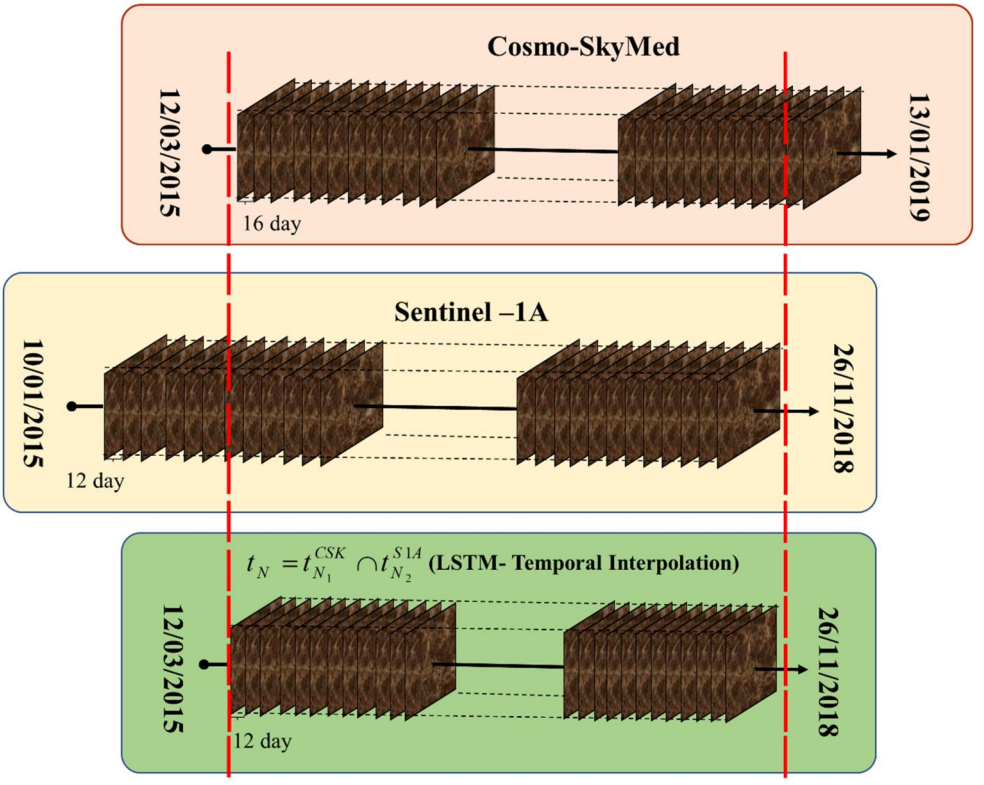

Figure 5. The methodology is to find the time interval and start and end date of temporal interpolation by the time interface of data collection.

Here, finding the time interval and start and end date of temporal interpolation was done at the time interface of data collection. Assuming the time series of each pixel is in the CSK dataset as $t_{N_1}^{CSK} = \{t_1, t_2, \ldots, t_{N_1}\}$, in the S1A dataset as $t_{N_2}^{S1A} = \{t_1, t_2, \ldots, t_{N_2}\}$, the intersection of these two datasets is defined as $t_N = t_{N_1}^{CSK} \cap t_{N_2}^{S1A} = \{t_1, t_2, \ldots, t_N\}$. In other words, to perform this temporal interpolation, we have considered the start and end times of the interpolation as $\max\{\min(t^{csk}), \min(t^{S1A})\}$ and $\min\{\max(t^{csk}), \max(t^{S1A})\}$, respectively. Then, the time intervals from the start date to the final date are set as 12 days. Note that in this temporal interpolation, both S1A and CSK data are interpolated on the new temporal grid (Figure 5).

The LSTM can be utilized here by training the network to find and predict the missing data in the new time-step (t_N), which we determine as the same time interval for all datasets based on learning of all old time-steps for each dataset separately. Then, we can feed the LSTM with actual data up to the time to generate the value for the missing time-step.

In our study, after hyperparameter tuning and training the LSTM model on the all-available time steps of each dataset, it was used to predict deformation for the new time-step (t_N). This approach allowed all two datasets to be synchronized to the same timeline, ensuring consistency and comparability across the datasets. Table 2

Table 2. Hyperparameter and parameter used in LSTM model for temporal interpolation.

Parameter	Value
Number of layers	3
Units per layer	50
Dropout rate	0.2
Recurrent Dropout rate	0.2
Optimizer	Adam
Learning rate	0.008
Batch size	32
Number of epochs	86

shows the important parameter we used for the temporal interpolation by the LSTM model after hyperparameter tuning. The presented LSTM model is configured with three layers, indicative of a design that seeks to balance depth with computational efficiency. Each layer houses 50 units, a moderate number that suggests an attempt to capture intricate temporal patterns while still retaining a manageable level of model complexity and computational demand. This structure enables the model to learn from and make predictions based on time-series data, which is essential for the task of temporal interpolation in this study. The careful calibration of the number of layers and units per layer reflects an effort to optimize the model's performance without succumbing to the problems of overfitting, especially critical in scenarios where training data may be limited or highly variable.

Regularization techniques are employed robustly within the LSTM architecture to further mitigate overfitting. A dropout rate and a recurrent dropout rate of 0.2 provide a systematic approach to reducing the model's complexity during training, effectively simplifying the model by ignoring a subset of the neurons. The use of the Adam optimizer with a specific learning rate of 0.008 is a strategic choice, as Adam is known for its adaptive learning capabilities and is adept at managing sparse gradients. The batch size is set at 32, a standard in the industry, balancing the benefits of stochastic gradient descent with computational efficiency. Training over 86 epochs, the model undergoes a thorough learning process, likely determined through trial and error to be the optimal duration for convergence without excessive computation. This careful selection of hyperparameters, including the learning rate and number of epochs, suggests a comprehensive fine-tuning process, tailoring the model to the unique requirements of accurately capturing and interpreting the temporal evolution of landslide deformation.

Spatial interpolation using CNN: With the two different satellite-derived datasets (CSK and S1A), we applied a robust and adaptive CNN to solve the spatial interpolation problem.

The structure and functioning of a CNN allow it to analyze and interpret spatial data. It features three types of layers, each bringing its unique functionalities to the fore: convolutional layers, pooling layers, and fully connected layers. In conjunction, they facilitate a robust understanding of spatial patterns in data and are, therefore, aptly suited for spatial interpolation tasks.

CNNs excel in hierarchical feature learning. Given the spatial nature of InSAR data, there are likely local patterns (like specific deformation signatures) and more global trends (like overall landslides movement). CNNs, with their convolutional

layers, can extract these multi-level spatial features effectively (Zhang et al. 2020). One of the strengths of CNNs is their ability to recognize patterns regardless of their position in the input space. For InSAR spatial data, this means that a specific deformation pattern can be recognized by the CNN irrespective of where it appears in the datasets obtained from CSK and S1A (Brengman and Barnhart 2021). The architecture of CNNs involves sharing weights across spatial locations. This not only reduces the number of parameters, making the model more efficient, but also ensures that a particular feature can be detected anywhere in the input, further emphasizing its application for spatial interpolation of InSAR data.

CNN layer information, definitions, and equations can be found in Ghosh et al. (2020).

In our study, the data from S1A and CSK were resampled into a pre-defined grid to ensure uniformity and consistency across datasets. The resampling was an essential preparatory step to make the data amenable to synergistic integration. As mentioned before, the spatial interpolation utilizing a CNN was performed on structured data extracted and pre-processed from S1A and CSK datasets rather than directly on imagery. We adapted the Bilinear Interpolation technique (Peng et al. 2021) to suit our dataset's unique structure for the critical step of resampling the data extracted from CSK and S1A images and compiled into Excel files. While traditionally applied to pixel values in images, the principles of Bilinear Interpolation were creatively repurposed to calculate new cumulative deformation values based on a weighted average of spatially adjacent data points within our Excel datasets.

To facilitate the CNN algorithm's application, this data was resampled into a predefined grid, ensuring that the datasets could be uniformly and consistently integrated despite originating from different satellite sources. The objective was to align the spatial properties of these datasets, creating a conducive environment for the CNN model to predict spatial deformation patterns accurately. It's essential to note that the pre-processing steps, including resampling, were geared towards achieving homogeneity in the input data for practical spatial analysis by the CNN model. While not visualized as images in our documentation, the resampled data served as the foundation for our spatial interpolation analysis, ultimately contributing to our comprehensive understanding of landslide kinematics.

Rather than using a simple weighted sum, which might compromise on retaining detailed features from each dataset, we utilized the convolutional layers of the CNN model. With its hierarchy of convolutional filters, CNN efficiently combined the datasets by extracting and preserving crucial features from each source. This approach ensured a comprehensive representation of the combined datasets, retaining unique details while leveraging the strengths of each dataset.

Boundaries play a crucial role in spatial interpolation, particularly in geospatial datasets like InSAR. The ability of CNNs to discern boundaries is attributed to the convolution operation, which can detect abrupt changes or transitions in spatial data. When a CNN processes geospatial data, the convolutional filters, especially those in the initial layers, act as edge detectors. These filters are trained to recognize differences in neighboring pixels or cells, marking out boundaries or transitions. As the spatial data progresses through more profound network layers, these detected boundaries

become integral features that the subsequent layers use to guide the spatial interpolation process. Furthermore, pooling layers within CNNs by Downsampling the input ensures that the model can recognize broader spatial patterns and not just localized features. This balance of recognizing minute details while being aware of larger spatial contexts aids CNN in accurately defining boundaries and executing spatial interpolation without introducing artifacts or unrealistic transitions.

Based on the learned spatial patterns, the fully connected layer assigns an interpolated value to each specific location on the optimized 2D grid. The multiple layers of the CNN model facilitated high-precision estimation of deformation in unobserved locations, culminating in a comprehensive understanding of our spatial domain. The critical hyperparameter of the size of the 2D grid was determined through an extensive cross-validation process.

The final act of this grand play was the CNN model performing spatial interpolation across our entire dataset, using the optimal grid size. This process concluded with generating high-precision deformation predictions for the spatial region of interest.

It is worth noting that training the CNN involves adjusting its parameters, which are the weights and biases of the filters in the convolutional layers and the connections in the fully connected layer. This is done *via* a method called backpropagation, which computes the gradient of the loss function concerning the network parameters and applies an optimization algorithm named Adam to minimize the loss function. Through these steps, the model learns the optimal parameters to estimate deformation in the spatial domain with high precision on the optimized 2D grid.

In Table 3, you can find the important parameter we used for the spatial interpolation by the CNN model. The CNN specified in the table is structured with three convolutional layers, indicating a design to capture complex features from the input data at multiple levels of abstraction. With 64 filters in each layer, the network is capable of identifying a wide array of features within the data, which could be essential for nuanced detection or classification tasks. The chosen filter size of 5×5 strikes a balance between detail and computational efficiency, allowing the CNN to effectively process spatial information without becoming bogged down by an excessive computational load. The application of 'Max' pooling suggests an intent to reduce dimensionality and prevent overfitting by summarizing the most prominent features within a pool window, thus ensuring the most significant attributes are retained for subsequent layers.

Table 3. Hyperparameter and parameter used in CNN model for spatial interpolation.

Parameter/Hyperparameter	Value
Convolutional layers	3
Number of layer's filters	64
Filter size	5×5
Pooling type	'Max'
Activation function	'ReLU'
Optimizer	'Adam'
Loss function	'Mean Squared Error'
Batch size	32
Epochs	100
Grid dimension	20.22 m

The CNN utilizes the 'ReLU' activation function to introduce non-linearity, a crucial feature for enabling the model to capture complex patterns and make predictions beyond the scope of linear models. The 'Adam' optimizer reflects a choice for adaptively tuning the learning rate to effectively handle a wide range of data dynamics. With 'Mean Squared Error' as the loss function, the model seems to be geared toward regression tasks, where minimizing the average of the squares of the differences between predicted and actual values is critical. Training is conducted with a batch size of 32, providing a compromise between the accuracy of the gradient estimate and memory efficiency. Over 100 epochs, this training regime allows the CNN to refine its weights thoroughly, adjusting and improving from the feedback of the data iteratively. Lastly, the specified grid dimension of 20.22 m indicates the spatial granularity of the analysis, a crucial factor in applications like remote sensing, where it determines the scale at which phenomena are observed and predictions are made.

The success of deep learning models hinges on systematic training and robust validation methodologies. For our study, we adopted a comprehensive process to ensure the LSTM and CNN models effectively analyze and interpolate the missing data of the new time frame and also the new boundary of the InSAR data. The dataset was partitioned into training, validation, and test sets, adopting an 80-10-10 split. The training set formed the foundational bedrock upon which our LSTM model was initially trained. Given the time-series nature of our dataset, LSTM was trained using sequences of cumulative deformation data, making certain the model grasped the inherent temporal dependencies and patterns. The sequence length was optimized (t_N) to maintain a harmony between recognizing long-term temporal trends and ensuring computational feasibility.

Upon extracting temporal patterns using LSTM, the CNN model took over to understand the spatial intricacies of the deformation. It analyzed spatial data chunks, ensuring a keen understanding of localized and expansive spatial deformation patterns. The convolutional layers, with varying kernel sizes, were trained to discern and differentiate between granular features and overarching spatial trends. Incorporated within both models were regularization strategies, like dropout layers, to avert overfitting. Early stopping, which monitored the validation loss, was another measure taken; curtailing the training once overfitting signs became evident, thus reinforcing model generalizability.

The validation set, constituting 10% of the data, acted as a periodic checkpoint throughout the training phase. After each epoch, the LSTM and the CNN models were assessed against this validation set. This iterative training and validation approach ascertained that the models were not only aligning with the training data nuances but also proficiently generalizing to novel data. Conclusively, the models were tested on the reserved 10% dataset upon reaching an optimized state, offering an extensive performance evaluation.

4.2.4. Re-projection synergic data with GPS stations

In the final stages of our methodology, after executing temporal interpolation *via* LSTM and spatial interpolation through CNN, we integrate our PS and DS points to form a unified grid file. Each data point is now characterized by its unique space,

time, and associated velocity coordinates, which have been determined with high precision through our robust interpolation. This critical unification, after having navigated through the complexities of diverse satellite datasets and irregular time and space intervals, is a significant step toward creating our final velocity map.

Following this, it is necessary to integrate the GPS station (M01) located in the stable area into our synthesized dataset. The GPS measurements serve as the bedrock for our spatial coordination, providing a reliable and accurate reference frame. We utilize these GPS readings to co-reference our DS and PS points, rectifying and refining our velocity estimates. The GPS data integration and the subsequent coordinate transformation allow for a spatially harmonized and consistent final velocity map. Indeed, to align Synergic and GPS datasets in same reference frames, the offset between them must be removed. So, for a selected stable GPS site, we calculate the Synergic-derived LoS values for pixels located within a circle radius around it. Then, the velocity of this GPS site is projected onto the LoS according to local incidence angles. So, we estimate a mean Synergic LoS rate inside a circle. Finally, the averaged value of offsets between GPS and Synergic is subtracted from all the Synergic observations.

5. Results

5.1. Mean deformation rate maps

Employing the SBAS technique with the S1A operating in the C-band, we noted considerable movement rates in the central region of the instability zone. Meanwhile, the upper sector exhibited lower rates, yet these rates were still indicative of significant movement (Figure 6). As far as the eastern sector is concerned, the most significant deformation rates were recorded in the upper sector, in correspondence, in this case, to the high density of buildings. It is noticed that the mean deformation rate maps obtained from SBAS and PSI were provided before spatial and temporal interpolation.

Complementing these findings, the CSK dataset, leveraging the X-band's high spatial resolution, provided more detail-oriented insights into landslide kinematics. Even though it operates with a narrower swath, the precise spatial information offered by the X-band presented a detailed picture of localized deformation patterns. The ability to capture minute changes in the urban landscapes was invaluable in characterizing the landslides' boundaries and internal kinematics (Figure 7). As in previous outcomes, although in this case, the targets are only concentrated at the urban area (characteristic of the X-band), again the highest deformation rates were found in the central sector at the university campus. However, the deformation in highway structure did not appear on this map due to the type of road, characterized by the absence of guardrails, which would ensure that the electromagnetic signal would return to the sensor and thus be identified.

These distinct datasets converged to provide a comprehensive view of landslide kinematics, each contributing a unique perspective. In fact, on the one hand, it is possible to identify two distinct phenomena, one in the westernmost and the other in the easternmost sector, characterized at their respective crowns by slightly different

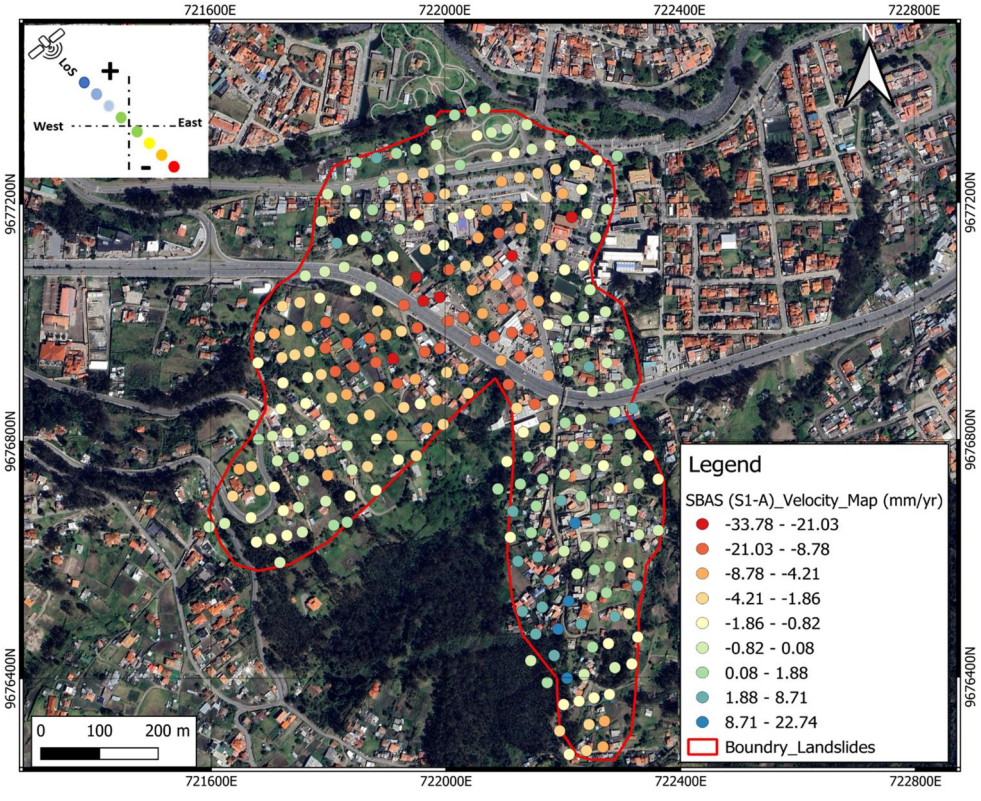

Figure 6. The mean deformation rate map along the LoS in ascending track according to SBAS (S1A).

deformation rates (indicate velocities). The distinction is also confirmed by the difference in sign found in the evaluation of the deformation rates, negative for the westernmost phenomenon and positive for the easternmost phenomenon, which also confirms the deformation directions of the phenomena. In fact, as is well known, for ascending data, positive values move toward the satellite in the East–West direction, while negative data moves away from the satellite in the West–East direction. Finally, the existence of the two different phenomena would seem to be further confirmed by the significant deformation rates found at the toe zone. Indeed, in this area, the confluence of the volumes involved in the two distinct phenomena generates an overlap of effects that gives rise to higher deformation rates. The observed variations across datasets underscore the importance of using multi-sensor and multi-technique approaches for a fundamental understanding of landslide phenomena.

5.2. Histogram of the velocity point scatterers

The data obtained from the PSI technique on CSK images represents the distribution of PS points at different velocities. Based on the graph obtained from this data (Figure 8a), it is clear that velocities range from −33 mm/yr to 14 mm/yr. Negative values signify eastward movement, while positive values represent westward

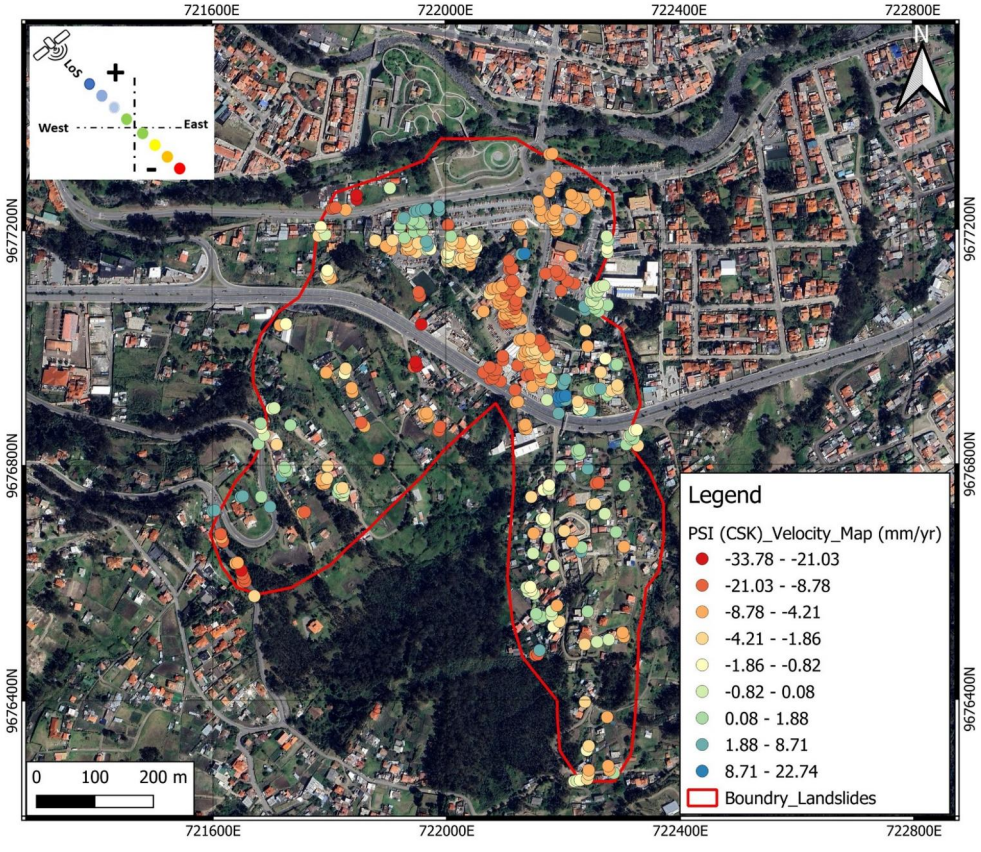

Figure 7. The mean deformation rate maps along the LoS in ascending track according to PSI (CSK).

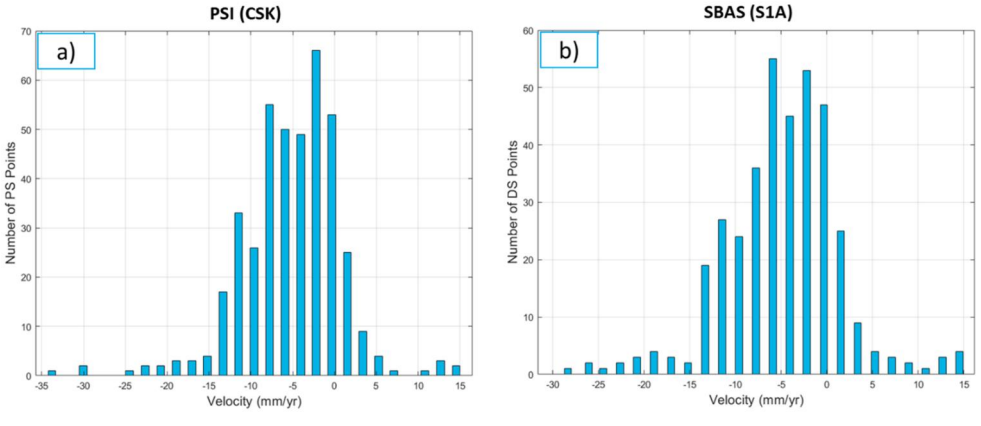

Figure 8. The histogram of scatterer points based on velocity includes a) PSI_CSK and b) SBAS_S1A.

movement. The highest frequency of PS points occurs at a velocity of −2mm/yr, suggesting that many features are moving at this velocity.

Fewer PS points are observed at both very high and very low velocities. For example, there is only one PS point at a velocity of −33 mm/yr and one at 10 mm/yr. This indicates that fewer geological features are moving at these extreme velocities. Most PS points (approximately 75.5%) fall within the −13 to 0 mm/yr velocity range. This suggests that most of the geological features under consideration are moving at these velocities. There is an evident skewness towards negative velocities, suggesting that most of the observed features move in the direction associated with these negative values.

As shown in Figure 8(b), obtained from S1A, respectively, provides the distribution of DS points across different velocities.

As with the previous data, velocities range from −28 mm/yr to 14 mm/yr. The negative and positive velocities suggest movement in two (west-east and east-west) directions, respectively. The highest number of DS points occurs at a velocity of −6 mm/yr, indicating that many features are moving at this velocity. The second highest number of DS points is at −2 mm/yr.

There are fewer DS points at both high positive and high negative velocities. Most DS points (i.e. approximately 74.2%) are concentrated within the velocity range from −13 to 0 mm/yr. This could indicate that the majority of features in the studied area are moving within these velocities. Like the PS data, there is an evident skewness towards negative velocities, indicating that most observed features are moving in the direction associated with these negative values.

5.3. Synergic mean deformation rate maps

A synergistic mean deformation rate map was generated upon integrating the individual results by applying spatial and temporal interpolation methods. The results deriving from the combination of the different processes allow some considerations to be made: on the one hand, the area affected by significant deformation rates could identify two different landslides, a first one with an SW-NE direction, characterized by greater deformation rates in the central sector, involving the university campus, a second landslide, on the other hand, with an S-N direction with significant deformation rates in the highest sector; however, a consideration lies in the results found in the downstream sector, where the positive values found would identify the accumulation zone of both landslides identified (Figure 9, left-top corner).

This collective approach enriched the spatial characteristics of the mean deformation map, enhancing the boundary of landslides, particularly in areas where the individual datasets may have been less effective alone. The integrated mean deformation rate map, depicting the spatial distribution of velocity changes over time, presented a unified perspective of landslide kinematics in both urban and rural landscapes. It highlighted potential areas of instability, tracing the kinematic evolution of these landslides and offering invaluable insights for risk assessment and landslides management (Figure 9).

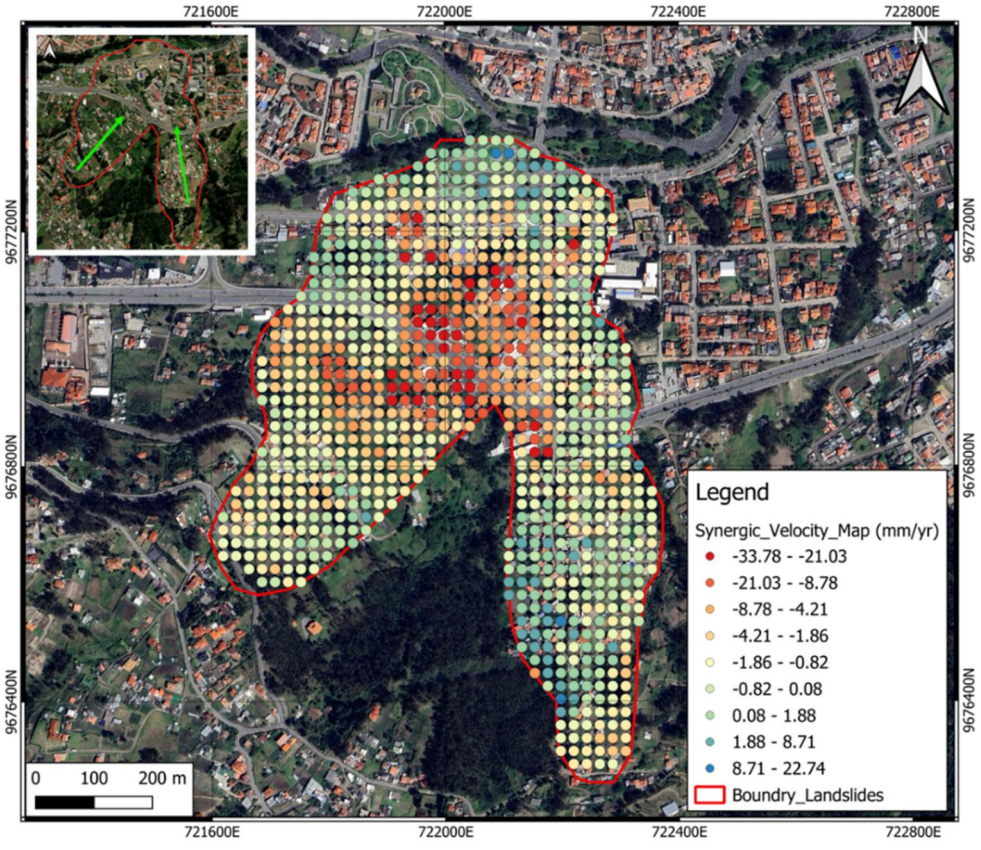

Figure 9. The mean deformation rate maps along the LoS in ascending track according to synergic datasets, including PSI (CSK) and SBAS (S1A).

As can be seen in Figure 10, the highest number of points occurs at a velocity of −3 mm/yr, suggesting that many features are moving at this velocity. The second highest number of points are at velocities −2 and −3 mm/yr, respectively. A substantial majority of points are concentrated within the velocity range from about −15 to 0 mm/yr. Specifically, 763 out of a total of 1010 points, or about 75.5%, are in this interval. This suggests that most of the geological features in the study area are moving at these velocities.

For a better understanding of the kinematic and temporal variation of the synergic result, Figure 11 has been provided. The left side of Figure 11 showcases a Synergic Velocity Map (with more details, coordinate and scale bar illustrated in Figure 9). This is overlaid on an aerial view of the area of interest and is marked with areas A, B, C, and D. Each area has a distinct color set based on the velocity scale presented in the legend.

- *Area A:* This is the area where the above two phenomena meet, causing significant deformation rates, probably due to overlapping effects. From a geological point of

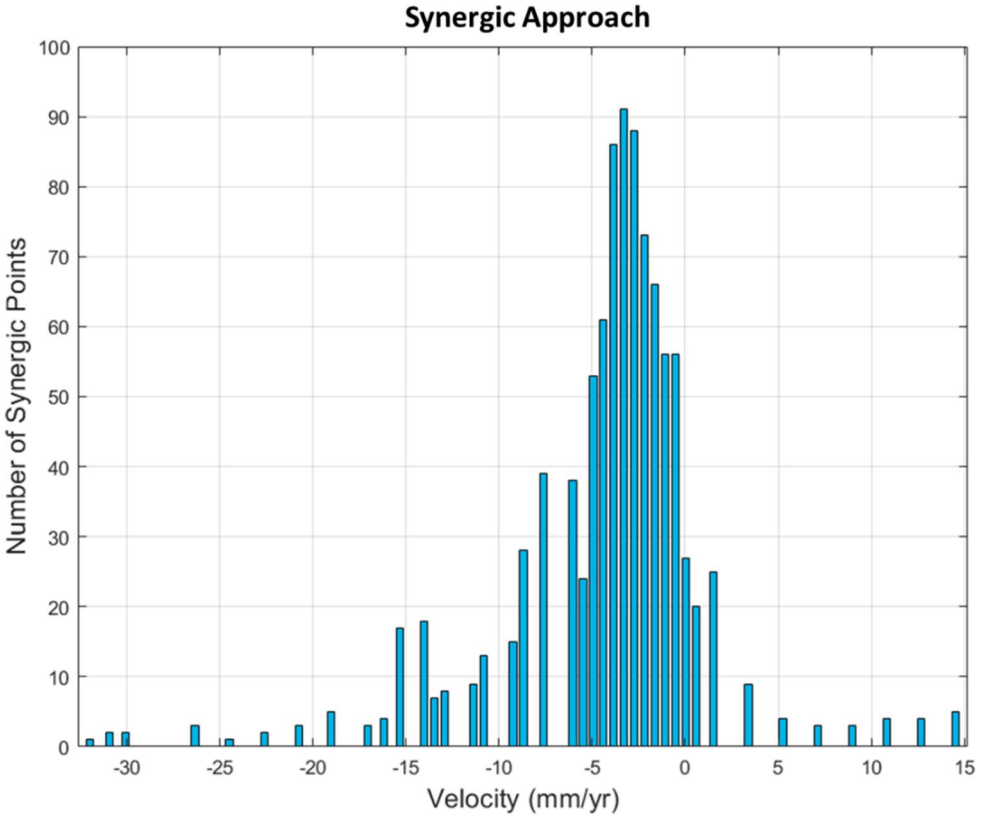

Figure 10. The histogram of scatterer points is based on the velocity of the synergic approach.

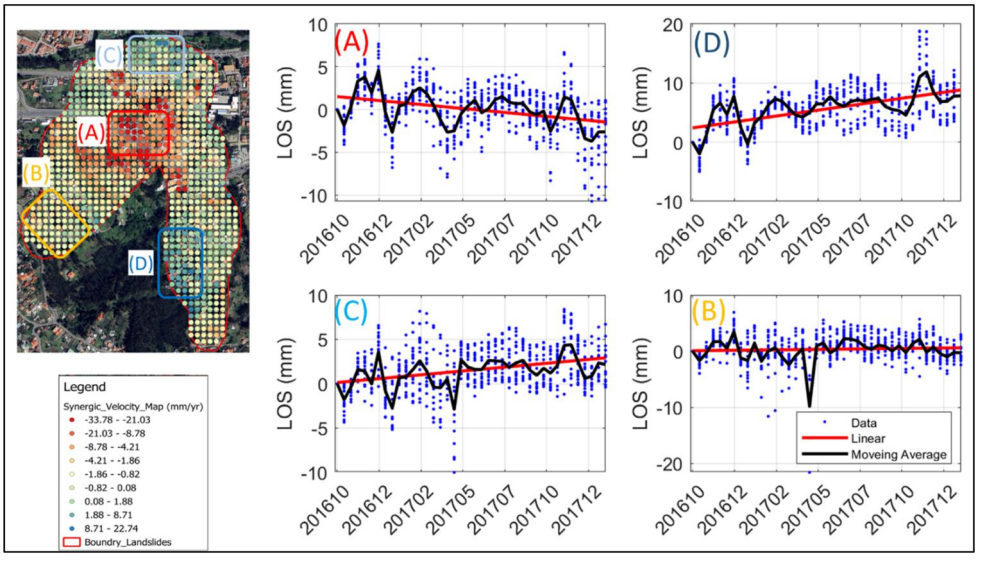

Figure 11. Temporal analysis of cumulative deformation obtained from Synergic approach.

view, the convoyed materials are at the contact between the Turi formation and the slope deposit.

- *Area B:* In the westernmost landslides' uppermost (crowning) sector, reduced deformation rates can be observed, indicating a more modest landslide activity involving materials (Turi Formation) that are not so poor from a mechanical point of view.
- *Area C:* In the crowning sector of the easternmost landslides, on the other hand, moderate rates of deformation are observed, thus indicating a range of activity. Confirming this also from a geological point of view, materials with definitely poorer mechanical properties classified as slope deposits are involved. The mostly lower velocities and the upward trend observed in the time-series graph suggest that this area is experiencing some recovery or rebound.
- *Area D:* Significant, albeit positive, values of deformation rates are recorded in this area. We are at the foot of landslide phenomena where materials are present from a mechanical point of view poorer. Also, from a morphological point of view, the sector is uplifting, thus indicating a possible rotational sliding phenomenon (Cascini et al. 2009).

Landslides can exhibit varied deformation patterns based on their stage of activity and the type of movement (e.g. translational, rotational, and block slides). The regions of rapid deformation (like Area A) represent areas of potential active sliding, where continuous monitoring would be crucial. Areas with varied deformation rates (like Area B) might indicate intermittent sliding zones or the base of landslides where deposition and compression occur. The uplift observed in Area C could be a sign of compensational uplift from a nearby sliding area.

In general, The region under observation is experiencing varied kinematics of deformation. While areas like A and D are primarily deforming downwards, Area C displays signs of uplift. Area B, on the other hand, remains relatively stable but with periodic fluctuations, which could be seasonal.

5.4. Validation by GPS stations

With the availability of measurements from nine different GPS stations, we can conduct a more detailed comparison between the InSAR-derived deformation rates and the ground truth data. Each GPS station provides information, as they are located in different areas with varying landslide behaviours and conditions. This comparative analysis underscores the potential of our synergic approach to provide a comprehensive understanding of landslide kinematics, as it integrates the strengths of the individual datasets and techniques.

Table 4 presents a comparative analysis between different techniques—SBAS (S1A), PSI (CSK), and the synergic approach—and the actual values measured at the GPS stations at nine locations. Each row represents a unique station, while each column specifies the deformation rates averaged across the time series that each method estimated at these stations. With its integrative ability, the synergic approach

Table 4. Comparison of deformation rates (mm/year) derived from SBAS (S1A), PSI (CSK), and the synergic approach, with actual values measured at nine GPS stations.

GPS station	CSK (mm/year)	S-1A (mm/year)	Synergic (mm/year)	Measured by GPS (mm/year)
M09	−4	−5	−6	−6
M10	−4	−10	−13	−12
M15	−2	−15	−17	−17
M17	−8	−2	−4	−5
M18	−9	−5	−7	−6
M19	−4	−3	−5	−4
M20	−7	−4	−7	−6
M22	−6	−5	−3	−2
M23	−11	−6	−9	−10
RMSE	6.05	2.33	**0.88**	_

consistently provides estimates that harmonize the values derived from the other techniques, demonstrating its capacity to assimilate their collective strengths.

For a better understanding of the temporal behavior of true GPS measurements and the time series obtained by CSK, S1A, and the Synergic Approach, Figure 12 has been provided. In this Figure, the trends of all four data sources in M09, M10, M15, M18, M20, and M23 stations appear reasonably consistent, indicating good agreement between the Synergic approach, CSK, S1A, and true GPS measurements. GPS measurements and the Synergic approach results show very close matches in these stations, suggesting that the Synergic approach provided a reliable estimation of ground deformation, closely mirroring the GPS readings. The results obtained from CSK and S1A data tend to be slightly above the GPS and Synergic lines but follow a similar trend, indicating some systematic offset or discrepancy but retaining the overall deformation pattern.

In station M17, the Synergic approach and GPS closely align, with S1A also showing a similar trend but with an offset. However, the CSK data starts aligning with the others but diverges around mid-2017. This divergence could be due to errors or artifacts in the CSK dataset or actual differences in the deformation detected by CSK.

In station M19, an attractive station as the Synergic, CSK, and S1A measurements oscillate and do not maintain a consistent trend throughout the period. The GPS data, however, maintains a relatively consistent downward trend. This discrepancy might suggest that the satellite-derived measurements (Synergic Approach, CSK, and S1A) could be influenced by factors that the GPS is not, or vice versa. It might be worth further investigating the causes of these oscillations.

In station M22, while all datasets start with an aligned trend, post-mid-2017, there is a clear divergence between the GPS/Synergic approach results and the CSK/S1A data results. This divergence could again be attributed to errors, artifacts, or actual variations in the deformation captured by the different methodologies.

In general, In most stations, there is a good agreement between the Synergic approach and the direct GPS measurements. This suggests that the Synergic approach is reliable for capturing the broad trends of ground deformation. There are instances where the CSK and S1A datasets show slight to moderate discrepancies compared to the GPS data. These differences might be due to the satellite data's inherent limitations, differences in processing, or actual variations in

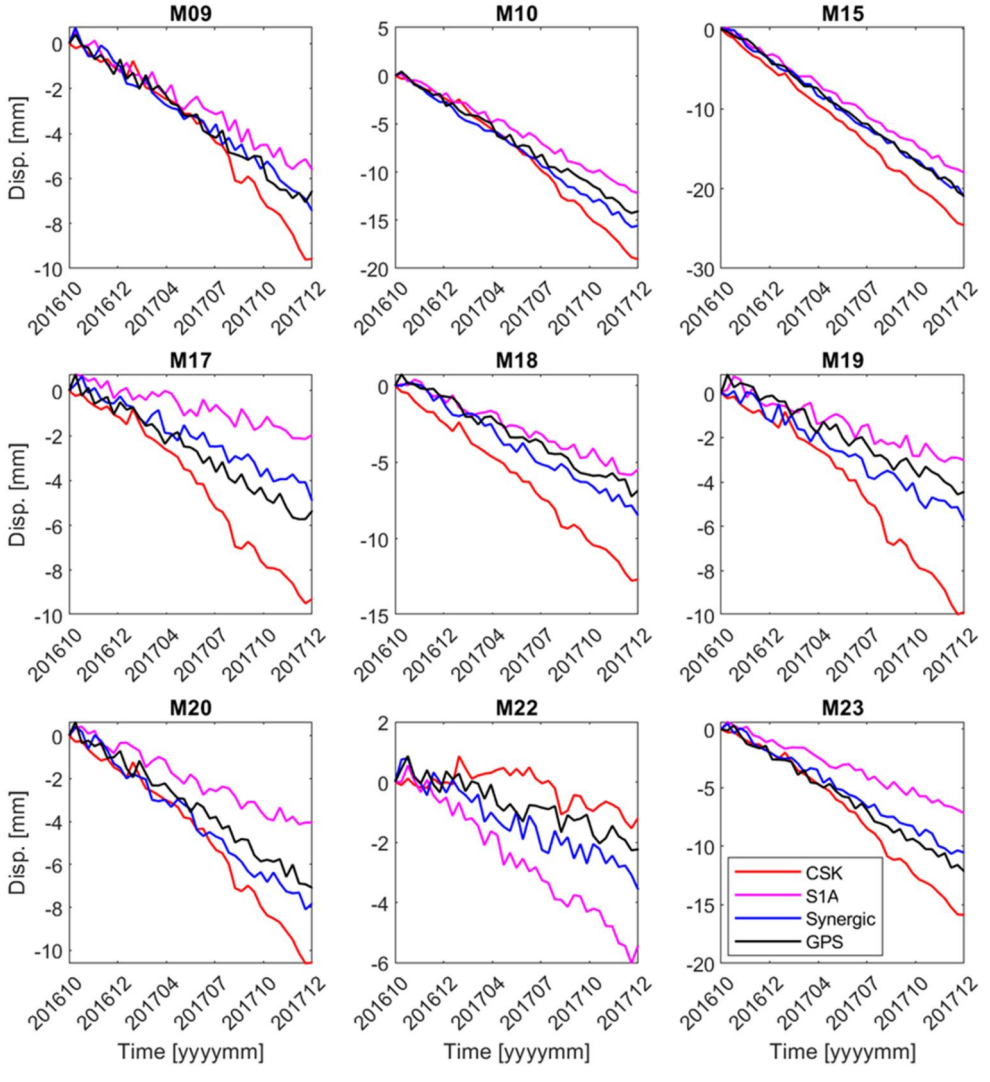

Figure 12. Comparison of time series deformation across nine GPS stations using Synergic approach, CSK, S1A, and direct GPS measurements.

deformation patterns captured by these satellites based on the location of the case study (urban and green area).

Note that, despite nine GPS points seem to be located in urban areas, which are expected to be more consistent with the deformation results exported from CSK data, however, upon comparing Figure 4 (which shows the locations of GPS stations) with Figure 7 (depicting measurement CSK points), it becomes evident that the CSK observations are notably absent in most of the GPS stations. Consequently, interpolation becomes necessary to construct CSK time series data, relying on neighboring points. Interestingly, the effect of this phenomenon is significantly less pronounced in the case of S1A observations. For instance, this difference is more pronounced at stations M19 and M20, where interpolation occurs over greater spatial distances. Conversely, the difference is much less at points like M22 and M23, where the interpolation spatial distance is smaller. Also, as

Table 5. Comparison of the percentage of cross-correlation from S1A, CSK, and the synergic approach, with actual values measured at nine GPS stations.

	Cross-correlation w.r.t GPS		
GPS station	CSK	S1A	Synergic
M09	97.98%	97.90%	98.46%
M10	99.10%	99.32%	99.52%
M15	99.86%	99.74%	99.76%
M17	98.57%	94.52%	96.95%
M18	98.81%	98.55%	98.34%
M19	97.34%	96.69%	97.24%
M20	98.43%	97.71%	98.70%
M22	71.40%	94.68%	92.19%
M23	99.24%	99.05%	99.29%
Mean	95.64%	96.57%	**97.83**%

mentioned before, the proximity of GPS observations to S1A observations is likely due to the reference setting of the angles in the Sentinel satellite's imaging geometry, facilitating the comparison of time series data along the satellite's LoS.

Table 5 offers a detailed comparison of the percentage of cross-correlation from three distinct satellite-based techniques—SBAS (S1A), PSI (CSK), and the synergic approach—with actual values measured at nine GPS stations. A closer look at the data for individual GPS stations reveals that For station M09, the Synergic approach outperforms the others with a correlation of 98.46%, closely followed by CSK at 97.98% and S1A at 97.90%. M10 and M15 demonstrate remarkable correlations across all methods, especially the Synergic approach that peaks at 99.52% for M10 and 99.76% for M15. At station M17, there is a noticeable variation, with CSK at 98.57%, the Synergic approach at 96.95%, and S1A lagging at 94.52%. The correlations for stations M18 and M19 are tightly packed, with all values hovering around the high 97% to 98% range. M20 showcases a strong performance for the Synergic approach at 98.70%. However, station M22 presents a stark deviation, especially for CSK, which dips to 71.40%, whereas S1A and the Synergic approach maintain a higher correlation of 94.68% and 92.19%, respectively. Lastly, M23 exhibits excellent correlations across the board, led by CSK at 99.24%.

The mean values, representing the average correlation across all nine stations, further underscore the performance of each method. While individual station data showed variations, the Synergic approach offers the highest mean correlation at 97.83% on average. S1A follows closely, with an average of 96.57%. The CSK method, despite its strong performance in several stations, is pulled down by its dip in M22, leading to an overall mean correlation of 95.64%.

In conclusion, the table underscores the efficacy of the Synergic approach in correlating with actual GPS measurements. It frequently rivals or surpasses the performance of both S1A and CSK, especially when considering the mean values. The data serves as a testament to the evolving precision of satellite-based deformation measurement techniques when benchmarked against ground-truth GPS data.

Table 6 shows the RMSE values obtained from time series' results of different methods and GPS observations. As it is evident, the time series deformation obtained using the Synergic Approach is more accurate than the other CSK and S1A datasets. In the Synergic Approach, the mean RMSE value was calculated as 0.77 mm, which is more accurate than the mean RMSE of the other methods.

Table 6. Comparison of RMSE obtained from S1A, CSK time series deformation, and the synergic approach, with actual values measured at nine GPS stations.

	RSEM w.r.t GPS		
GPS station	CSK	S1A	Synergic
M09	1.12	0.89	0.40
M10	2.30	1.44	0.94
M15	2.41	1.43	0.47
M17	2.05	2.31	0.88
M18	3.46	0.75	0.93
M19	2.97	0.76	0.90
M20	1.83	1.60	0.79
M22	0.80	2.18	0.77
M23	1.96	3.07	0.88
Mean	2.10	1.60	**0.77**

Our study found that integrating the S1A and CSK datasets with the SBAS and PSI techniques provided a comprehensive and precise perspective on landslide kinematics.

A notable limitation surfaced with the PSI technique when applied to the CSK dataset; it was less effective in detecting PS along highways and in green and rural environments. Using the synergistic approach provided an enhanced understanding of the landslides' direction and deformation pattern, reflecting the study area's geological setting. It accurately depicted the prevalent movement in the west-east direction and provided detailed information on the varying deformation rates across different locations.

Comparing our findings with prior research, the synergistic approach stood out due to its improved accuracy in investigating and analyzing landslides kinematics. Previous studies typically relied on a single-source SAR dataset and used a single processing technique, which may need to be more comprehensive to capture the complex kinematics of landslides. However, our synergistic approach proved more robust, yielding deformation rate estimates closer to the actual values measured by GPS stations. Based on the RMSE obtained from each technique and each dataset in comparison to the synergic approach, we have achieved an average improvement of 73% in the RMSE when compared to the measured values of the GPS station. The RMSE obtained from the synergic approach was improved compared with SBAS (S1A) and PSI (CSK) with 62.23% and 85.50%, respectively.

Furthermore, the observed correlation between landslide deformation rates and areas with high densities of buildings underscores the need for considering geohazards in urban planning and development.

5.5. Comparison between different interpolation results

This section offers a detailed comparison with synergic approach, illustrating the superior accuracy of deep learning approaches, especially when corroborated by GPS data. This sophisticated analysis highlights the advantages of using LSTM and CNN for landslides and sets a new benchmark for future research in this domain.

We evaluate the outcoming synergic results with two simple and well-known interpolation techniques, namely nearest neighbour, and kriging, to judge worth and compare the performances of our proposed method (Figure 13).

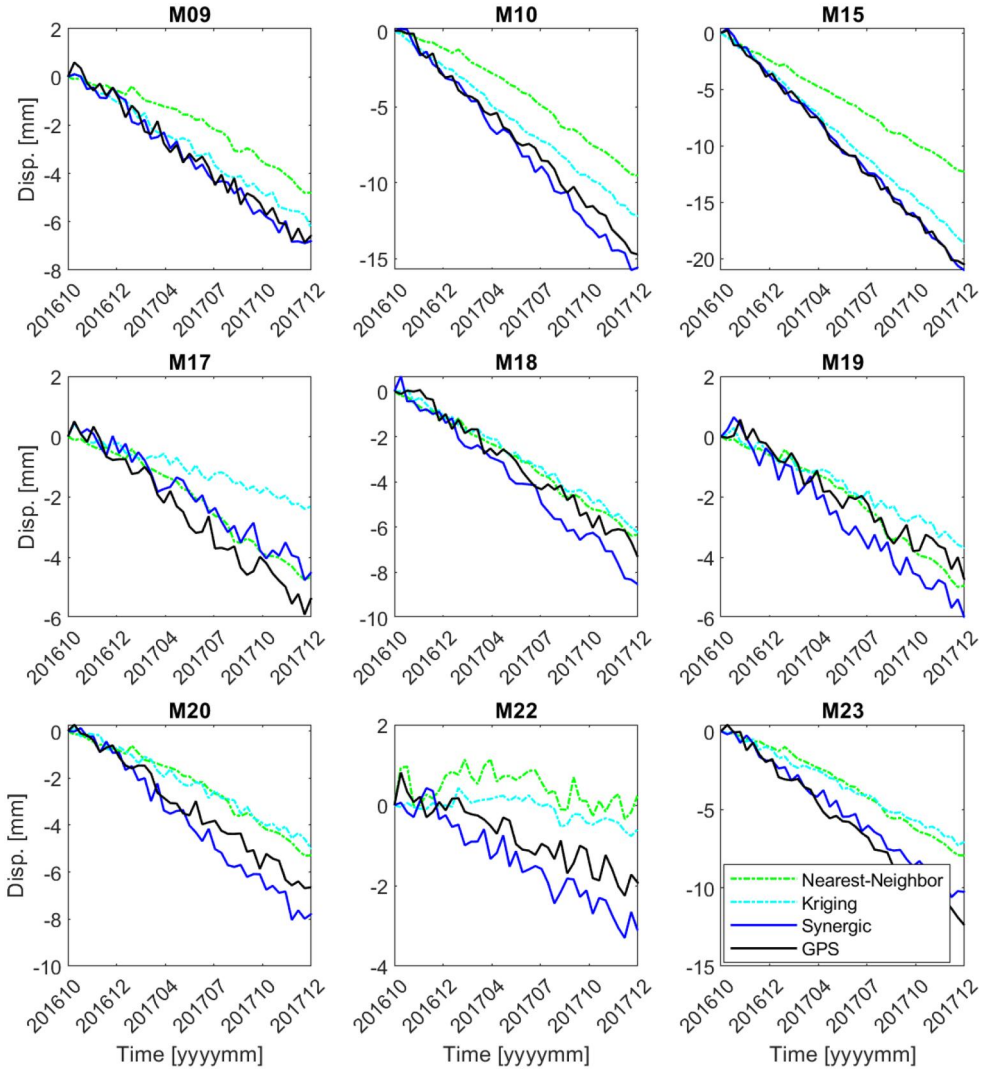

Figure 13. Comparison of time series deformation across nine GPS stations using synergic, nearest-neighbour, kriging interpolations, and direct GPS measurements.

Table 7 shows the RMSE values obtained from time series' results of different aforementioned methods and GPS observations. As it is evident, the time series deformation obtained using the Synergic Approach is very close to GPS observations. In the Synergic Approach, the mean RMSE value was calculated as 0.77 mm, which is more accurate than the mean RMSE of the other interpolation methods (Table 7).

6. Discussion

This study successfully integrated SAR satellite data and deep learning models to investigate active landslides in Cuenca, Ecuador, demonstrating the potential of combining advanced remote sensing techniques and different SAR imagery with machine learning for geohazard monitoring. However, it is crucial to critically analyze the

Table 7. Comparison of RMSE obtained from nearest-neighbour, Kriging interpolations, and the synergic approach, with actual values measured at nine GPS stations.

	RSEM w.r.t GPS		
GPS station	Nearest-neighbor	Kriging	Synergic
M09	1.56	0.59	0.40
M10	3.31	1.38	0.94
M15	5.01	1.32	0.47
M17	0.75	2.03	0.88
M18	0.49	0.64	0.93
M19	0.43	0.57	0.90
M20	1.16	1.25	0.79
M22	0.94	1.32	0.77
M23	2.59	2.80	0.88
Mean	1.80	1.32	**0.77**

strengths and limitations of our approach to provide a comprehensive understanding of its implications and prospects.

The primary strength of our approach lies in the synergistic use of multi-source SAR datasets (S1A and CSK) and advanced deep learning algorithms (LSTM and CNN). By leveraging the complementary strengths of the C-band and X-band imagery, we achieved a more comprehensive spatial and temporal understanding of the landslide dynamics. The LSTM model effectively addressed the temporal discrepancies between the datasets, ensuring a uniform 12-day time interval for analysis. The CNN model facilitated high-precision spatial interpolation, enabling us to generate detailed deformation maps with improved accuracy. This integration significantly enhances the capability to monitor slow-moving landslides in both urban and rural areas, as highlighted by previous studies (Crosetto et al. 2016; Di Napoli et al. 2023; Khalili et al. 2023).

The utilization of MT-InSAR techniques, such as PSI and SBAS, has allowed for the continuous monitoring of surface deformations with high precision. PSI, in particular, is adept at detecting small movements over long periods, especially in urban areas where stable scatterers like buildings are prevalent (Ferretti et al. 2001; Colesanti et al. 2003). On the other hand, SBAS is more effective in rural or vegetated areas where distributed scatterers are more common (Berardino et al. 2002). By combining these techniques with deep learning models, we have capitalized on the strengths of both methods, thereby providing a more holistic view of the landslide processes. Researchers have been trying to combine the two techniques for processing PSI and SBAS interferometric data for several years. On the one side by implementing processing chains as in the case of Ferretti et al. (2011) and Hooper (2008), and on the other side by using the data derived from different processing in a combined manner by integration, but in post-processing (Gama et al. 2019). In this work, an attempt was made to combine the results of the two techniques through the application of ML algorithms to obtain more robust results to better describe from a spatial and temporal point of view the phenomenon at hand.

Despite the promising results, our approach has certain limitations. Firstly, the accuracy of the interpolated results depends on the quality and density of the input data. In regions with sparse data points, the interpolation accuracy may decrease, potentially leading to less reliable deformation estimates. The temporal and spatial

resolutions of the SAR datasets are also limiting factors. For instance, while the CSK data provides high spatial resolution, its temporal resolution is lower compared to S1A, which can lead to challenges in capturing rapid deformation events (Di Martire et al. 2016). In addition, the complexity of deep learning models such as LSTM and CNN requires extensive computational resources and expertise in model training and validation, which may not be readily available to all researchers.

Future research should aim to address these limitations by exploring methods to enhance data density and quality, particularly in areas with sparse observations. Advanced techniques such as data fusion, where multiple types of geospatial data are integrated, could improve model performance and reduce computational requirements (Hu et al. 2020). Incorporating additional geospatial data sources, such as high-resolution optical imagery and ground-based measurements, could further refine the spatial and temporal accuracy of the deformation maps (Mohan et al. 2021).

Moreover, there is potential in utilizing transfer learning and domain adaptation techniques to apply models trained in one region to another, thereby enhancing the generalizability of the approach (Goodfellow et al. 2016). Extending the analysis to include different types of geohazards and environmental conditions will enhance the versatility and applicability of the methods developed in this study. Additionally, developing hybrid models that combine machine learning with physical models of landslide processes could provide more robust and interpretable results (Rivas-Medina et al. 2018).

In summary, while our study demonstrates significant advancements in landslide monitoring through the integration of SAR data and deep learning models, ongoing efforts to refine the methodology and address its limitations are essential for broader application and increased reliability. This research not only contributes to the scientific understanding of landslide dynamics but also provides a robust framework for future studies aimed at improving geohazard monitoring and risk mitigation.

7. Conclusion

Our research aimed to investigate using multi-source SAR datasets, including S1A and CSK, to understand and monitor landslide phenomena better.

We completely understood landslide movement through a multi-technique and multi-dataset approach. C-band imagery (S1A) proved better for analyzing landslide activity in mainly vegetated regions, while X-band imagery (CSK) was helpful in urban areas. In fact, on the one hand, the integrated analysis allowed us to identify more precisely the areal extension of the two landslides. The latter affects both intensely urbanized portions of the territory (foot or accumulation zone) and predominantly rural sectors of the slope (crown or upstream portion of the slope). On the other hand, it also allowed us to highlight differentiated deformation rates within the two identified landslides, recording higher rates in the lower middle sector of the westernmost landslides and similarly significant rates in the upstream sector of the easternmost landslides.

Additionally, we revealed an interesting pattern in the deformation direction based on the geological setting, with a prevalent SW-NE and S-N movement observed.

Furthermore, DLAs were instrumental in deriving a mean deformation rate map, revealing a new potential avenue for geohazard monitoring.

Also, From the velocity garnered through each method and dataset, compared to the synergic approach, the average improvement of 73.86% in the RMSE relative to the observed values from the GPS station was received.

This research lays the groundwork for a new investigation in landslide monitoring, highlighting the effectiveness of integrating multiple SAR datasets, diverse processing techniques, and DLAs. Our work emphasizes that the future of geohazard monitoring is likely to be increasingly interdisciplinary and technologically innovative, potentially leading to more robust and accurate risk assessment methodologies. Also, for future research, it is suggested to focus on retrieving deformation in the east, south, and up directions, based on the combination of some other SAR sources (such as ALOS or Sentinel-1A descending orbits), which is more practical and meaningful compared to LOS direction.

Acknowledgments

This study was carried out within the RETURN Extended Partnership and received funding from the European Union Next-Generation EU (National Recovery and Resilience Plan – NRRP, Mission 4, Component 2, Investment 1.3 – D.D. 1243 2/8/2022, PE0000005). The project was carried out using COSMO-SkyMed Products© of the Italian Space Agency (ASI), delivered under a license to use by ASI.

Authors' contributions

M.A.K: Conceptualization, Methodology, Software, Formal analysis, Investigation, Data curation, Writing- Original draft preparation, Visualization. S.C: Methodology, Software, Data curation, Writing- Original draft preparation, Visualization. D.C: Validation, Data curation, Investigation, Writing - Review & Editing. D.D.M: Conceptualization, Validation, Resources, Visualization, Writing - Review & Editing, Supervision.

Disclosure statement

No potential conflict of interest was reported by the author(s).

Funding

The Ph.D. project is funded according to Art. 4 L.210/98 and the University's Ph.D. regulations. Scientific Responsible Prof. Diego Di Martire.

ORCID

Mohammad Amin Khalili http://orcid.org/0000-0001-9671-761X
Silvio Coda http://orcid.org/0000-0003-2744-4771
Domenico Calcaterra http://orcid.org/0000-0002-3480-3667
Diego Di Martire http://orcid.org/0000-0003-0046-9530

Data availability statement

The datasets used and/or analyzed during the current study are available from the corresponding author upon reasonable request.

References

Agram PS, Gurrola EM, Lavalle M, Sacco GF, Rosen PA. 2016. The InSAR Scientific Computing Environment (ISCE): an Earth Science SAR Processing Framework, Toolbox, and Foundry. 2016: g 43A-1039.

Amin Khalili M, Di Muro C, Guerriero L, Ramondini M, Calcaterra D, Di Martire D. 2024. Evaluating the Effectiveness of Deep Learning Algorithms and InSAR Data in Early Warning Systems for Landslide Risk Mitigation [Internet]. [accessed 2024 Jul 15]; p107–113. doi: 10.18485/resylab.2024.6.ch13.

Ammirati L, Mondillo N, Rodas RA, Sellers C, Di Martire D. 2020. Monitoring land surface deformation associated with gold artisanal mining in the Zaruma City (Ecuador). Remote Sens. 12(13):2135. doi: 10.3390/rs12132135.

Babaee S, Khalili MA, Chirico R, Sorrentino A, Di Martire D. 2024. Spatiotemporal characterization of the subsidence and change detection in Tehran plain (Iran) using InSAR observations and Landsat 8 satellite imagery. Remote Sens Appl Soc Environ. 36:101290. doi: 10.1016/j.rsase.2024.101290.

Bausilio G, Khalili MA, Virelli M, Di Martire D. 2024. Italian COSMO-SkyMed atlas: R -Index and the percentage of measurability of movement. GIScience Remote Sens. 61(1): 2312705. doi: 10.1080/15481603.2024.2312705.

Berardino P, Fornaro G, Lanari R, Sansosti E. 2002. A new algorithm for surface deformation monitoring based on small baseline differential SAR interferograms. IEEE Trans Geosci Remote Sensing. 40(11):2375–2383. doi: 10.1109/TGRS.2002.803792.

Bonano M, Manunta M, Pepe A, Paglia L, Lanari R. 2013. From previous C-band to new X-band SAR systems: assessment of the DInSAR mapping improvement for deformation time-series retrieval in urban areas. IEEE Trans Geosci Remote Sensing. 51(4):1973–1984. doi: 10.1109/TGRS.2012.2232933.

Bonnet R-M, Manno V. 1994. International cooperation in space: the example of the European space agency. Cambridge: Harvard University Press.

Bovenga F, Candela L, Casu F, Fornaro G, Guzzetti F, Lanari R, Nitti DO, Nutricato R, Reale D. 2010. The COSMO SKYMED constellation turn on the L'Aquila earthquake: DInSAR results of the MORFEO project. In: [place unknown]p. 4803–4806. doi: 10.1109/IGARSS.2010.5654016.

Brengman CMJ, Barnhart WD. 2021. Identification of surface deformation in InSAR using machine learning. Geochem Geophys Geosyst. 22(3):e2020GC009204. doi: 10.1029/2020GC009204.

Busquier M, Lopez-Sanchez JM, Ticconi F, Floury N. 2022. Combination of time series of L-, C-, and X-band SAR images for land cover and crop classification. IEEE J Sel Top Appl Earth Observations Remote Sensing. 15:8266–8286. doi: 10.1109/JSTARS.2022.3207574.

Cascini L, Fornaro G, Peduto D. 2009. Analysis at medium scale of low-resolution DInSAR data in slow-moving landslide-affected areas. ISPRS J Photogramm Remote Sens. 64(6):598–611. doi: 10.1016/j.isprsjprs.2009.05.003.

Chen CW, Zebker HA. 2001. Two-dimensional phase unwrapping with use of statistical models for cost functions in nonlinear optimization. J Opt Soc Am A Opt Image Sci Vis. 18(2): 338–351. doi: 10.1364/josaa.18.000338.

Chen Y, He Y, Zhang L, Chen Y, Pu H, Chen B, Gao L. 2021. Prediction of InSAR deformation time-series using a long short-term memory neural network. Int J Remote Sens. 42(18):6919–6942. doi: 10.1080/01431161.2021.1947540.

Chini M, Albano M, Saroli M, Pulvirenti L, Moro M, Bignami C, Falcucci E, Gori S, Modoni G, Pierdicca N, et al. 2015. Coseismic liquefaction phenomenon analysis by COSMO-SkyMed: 2012 Emilia (Italy) earthquake. Int J Appl Earth Obs Geoinformation. 39:65–78. doi: 10.1016/j.jag.2015.02.008.

Colesanti C, Ferretti A, Prati C, Rocca F. 2003. Monitoring landslides and tectonic motions with the permanent scatterers technique. Eng Geol. 68(1–2):3–14. doi: 10.1016/S0013-7952(02)00195-3.

Crosetto M, Monserrat O, Cuevas-González M, Devanthéry N, Crippa B. 2016. Persistent scatterer interferometry: a review. ISPRS J Photogramm Remote Sens. 115:78–89. doi: 10.1016/j.isprsjprs.2015.10.011.

Das S, Mallik J, Dhankhar S, Suthar N, Singh AK, Dutta V, Gupta U, Kumar G, Singh R. 2020. Application of fracture induced electromagnetic radiation (FEMR) technique to detect landslide-prone slip planes. Nat Hazards. 101(2):505–535. doi: 10.1007/s11069-020-03883-3.

Del Soldato M, Confuorto P, Bianchini S, Sbarra P, Casagli N. 2021. Review of works combining GNSS and InSAR in Europe. Remote Sens. 13(9):1684. doi: 10.3390/rs13091684.

Delgado Blasco JM, Foumelis M, Stewart C, Hooper A. 2019. Measuring urban subsidence in the Rome Metropolitan Area (Italy) with Sentinel-1 SNAP-StaMPS persistent scatterer interferometry. Remote Sens. 11(2):129. doi: 10.3390/rs11020129.

Di Martire D, Tessitore S, Brancato D, Ciminelli MG, Costabile S, Costantini M, Graziano GV, Minati F, Ramondini M, Calcaterra D. 2016. Landslide detection integrated system (LaDIS) based on in-situ and satellite SAR interferometry measurements. CATENA. 137:406–421. doi: 10.1016/j.catena.2015.10.002.

Di Napoli M, Miele P, Guerriero L, Annibali Corona M, Calcaterra D, Ramondini M, Sellers C, Di Martire D. 2023. Multitemporal relative landslide exposure and risk analysis for the sustainable development of rapidly growing cities. Landslides. 20(9):1781–1795. doi: 10.1007/s10346-023-02065-z.

Dong Z, Wang G, Amankwah SOY, Wei X, Hu Y, Feng A. 2021. Monitoring the summer flooding in the Poyang Lake area of China in 2020 based on Sentinel-1 data and multiple convolutional neural networks. Int J Appl Earth Obs Geoinformation. 102:102400. doi: 10.1016/j.jag.2021.102400.

Esmaeeli N, Sattari F, Lefsrud L, Macciotta R. 2023. Assessing the risks associated with the Canadian railway system using a safety risk model approach. Transp Res Rec.: 036119812311765. doi: 10.1177/03611981231176549.

Covello F, Battazza F, Coletta A, Lopinto E, Fiorentino C, Pietranera L, Valentini G, Zoffoli S. 2010. COSMO-SkyMed an existing opportunity for observing the Earth. J Geodyn. 49(3-4):171–180. doi: 10.1016/j.jog.2010.01.001.

Ferretti A, Fumagalli A, Novali F, Prati C, Rocca F, Rucci A. 2011. A new algorithm for processing interferometric data-stacks: SqueeSAR. IEEE Trans Geosci Remote Sensing. 49(9):3460–3470. doi: 10.1109/TGRS.2011.2124465.

Ferretti A, Prati C, Rocca F. 2001. Permanent scatterers in SAR interferometry. IEEE Trans Geosci Remote Sensing. 39(1):8–20. doi: 10.1109/36.898661.

Franceschetti G, Lanari R. 1999. Synthetic aperture radar processing. Boca Raton: CRC Press.

Gabriel AK, Goldstein RM, Zebker HA. 1989. Mapping small elevation changes over large areas: differential radar interferometry. J Geophys Res. 94(B7):9183–9191. doi: 10.1029/JB094iB07p09183.

Gama FF, Paradella WR, Mura JC, de Oliveira CG. 2019. Advanced DINSAR analysis on dam stability monitoring: a case study in the Germano mining complex (Mariana, Brazil) with SBAS and PSI techniques. Remote Sens Appl Soc Environ. 16:100267. doi: 10.1016/j.rsase.2019.100267.

Ghosh A, Sufian A, Sultana F, Chakrabarti A, De D. 2020. Fundamental Concepts of Convolutional Neural Network. In: Balas VE, Kumar R, Srivastava R, editors. Recent trends adv artif intell internet things [Internet]. Cham: Springer International Publishing; [accessed 2023 Aug 18]. p. 519–567. doi: 10.1007/978-3-030-32644-9_36.

Goodfellow I, Bengio Y, Courville A. 2016. Deep learning. Cambridge: MIT Press.

Guerriero L, Confuorto P, Calcaterra D, Guadagno FM, Revellino P, Di Martire D. 2019. PS-driven inventory of town-damaging landslides in the Benevento, Avellino and Salerno Provinces, Southern Italy. J Maps. 15(2):619–625. doi: 10.1080/17445647.2019.1651770.

Guzzetti F, Mondini AC, Cardinali M, Fiorucci F, Santangelo M, Chang K-T. 2012. Landslide inventory maps: new tools for an old problem. Earth-Sci Rev. 112(1-2):42–66. doi: 10.1016/j.earscirev.2012.02.001.

Hanssen RF, Ferretti A. 2002. Parameter estimation in PS-InSAR deformation studies using integer least-squares techniques. 2002: g 62A-06.

Hochreiter S, Schmidhuber J. 1996. LSTM can Solve Hard Long Time Lag Problems. In: Adv Neural Inf Process Syst [Internet]. Vol. 9. Cambridge: MIT Press; [accessed 2023 Jul 19]. https://proceedings.neurips.cc/paper/1996/hash/a4d2f0d23dcc84ce983ff9157f8b7f88-Abstract.html.

Hooper A, Zebker H, Segall P, Kampes B. 2004. A new method for measuring deformation on volcanoes and other natural terrains using InSAR persistent scatterers. Geophys Res Lett [Internet]. 31(23). [accessed 2023 Jan 29] doi: 10.1029/2004GL021737.

Hooper A. 2008. A multi-temporal InSAR method incorporating both persistent scatterer and small baseline approaches. Geophys Res Lett [Internet]. 35(16). [accessed 2023 Jan 29]. doi: 10.1029/2008GL034654.

Hu Y, Xu X, Wu F, Sun Z, Xia H, Meng Q, Huang W, Zhou H, Gao J, Li W, et al. 2020. Estimating forest stock volume in Hunan province, china, by integrating in situ plot data, sentinel-2 images, and linear and machine learning regression models. Remote Sens. 12(1):186. doi: 10.3390/rs12010186.

Hungerbühler D, Steinmann M, Winkler W, Seward D, Egüez A, Peterson DE, Helg U, Hammer C. 2002. Neogene stratigraphy and Andean geodynamics of southern Ecuador. Earth-Sci Rev. 57(1-2):75–124. doi: 10.1016/S0012-8252(01)00071-X.

Iglesias R, Mallorqui JJ, Monells D, López-Martínez C, Fabregas X, Aguasca A, Gili JA, Corominas J. 2015. PSI deformation map retrieval by means of temporal sublook coherence on reduced sets of SAR images. Remote Sens. 7(1):530–563. doi: 10.3390/rs70100530.

Jiang H, Balz T, Cigna F, Tapete D, Li J, Han Y. 2023. Multi-sensor InSAR time series fusion for long-term land subsidence monitoring. Geo-Spat Inf Sci. 0(0):1–17. doi: 10.1080/10095020.2023.2178337.

Khalili MA, Bausilio G, Di Muro C, Zampelli SP, Di Martire D. 2023. Investigating gravitational slope deformations with COSMO-SkyMed-based differential interferometry: a case study of San Marco dei Cavoti. Appl Sci. 13(10):6291. doi: 10.3390/app13106291.

Khalili MA, Guerriero L, Coda S, Sellers C, Calcaterra D, Martire DD. 2023. Assessment of MT-InSAR processing techniques for slow-moving landslides monitoring in Cuenca (Ecuador) through double-band SAR satellite. Ital J Eng Geol Environ.:81–88. doi: 10.4408/IJEGE.2023-01.S-11.

Khalili MA, Guerriero L, Pouralizadeh M, Calcaterra D, Di Martire D. 2023. Monitoring and prediction of landslide-related deformation based on the GCN-LSTM algorithm and SAR imagery. Nat Hazards. 119[accessed 2023 Sep 9(1):39–68. doi: 10.1007/s11069-023-06121-8.

Khalili MA, Palumbo S, Madadi S, Bausilio G, Voosoghi B, Calcaterra D, Di Martire D. 2024. Enhancing landslide prediction through advanced transformer-based models: integrating SAR imagery and environmental data. E-J Nondestruct Test [Internet]. 29(07). [accessed 2024 Jul 15] doi: 10.58286/29721.

Kong Y-L, Huang Q, Wang C, Chen J, Chen J, He D. 2018. Long Short-Term Memory Neural Networks for online disturbance detection in satellite image time series. Remote Sens. 10(3):452. doi: 10.3390/rs10030452.

Kumar V, Venkataramana G, Høgda KA. 2011. Glacier surface velocity estimation using SAR interferometry technique applying ascending and descending passes in Himalayas. Int J Appl Earth Obs Geoinformation. 13(4):545–551. doi: 10.1016/j.jag.2011.02.004.

Lanari R, Mora O, Manunta M, Mallorqui JJ, Berardino P, Sansosti E. 2004. A small-baseline approach for investigating deformations on full-resolution differential SAR interferograms. IEEE Trans Geosci Remote Sensing. 42(7):1377–1386. doi: 10.1109/TGRS.2004.828196.

Li S, He S, Yue T, Du Z, Zhao N, Zhao Y, Jiao Y, Fan B, Liu Y, Xu Z, et al. 2023. Mapping bamboo forest and expansion intensity in China by coupling vegetation phenology and C-band SAR with Sentinel-1 and Sentinel-2 images. Int J Appl Earth Obs Geoinformation. 121:103384. doi: 10.1016/j.jag.2023.103384.

Lin D, Guoxiang LIU, Rui Z, Xiaowen W, Bing YU, Jia T, Heng Z. 2016. A multi-platform MC-SBAS method for extracting long-term ground deformation. Acta Geod Cartogr Sin. 45(2):213. doi: 10.11947/j.AGCS.2016.20140614.

Litherland M. 1994. The metamorphic belts of Ecuador. Overseas Mem Br Geol Surv. 11:1–147.

Liu Z, Shi W, Yu Y, Chen P, Yu Chen B. 2022. A LSTM-based approach for modelling the movement uncertainty of indoor trajectories with mobile sensing data. Int J Appl Earth Obs Geoinformation. 108:102758. doi: 10.1016/j.jag.2022.102758.

Miele P, Di Napoli M, Guerriero L, Ramondini M, Sellers C, Annibali Corona M, Di Martire D. 2021. Landslide Awareness System (LAwS) to increase the resilience and safety of transport infrastructure: the case study of Pan-American highway (Cuenca–Ecuador). Remote Sens. 13(8):1564. 1564. doi: 10.3390/rs13081564.

Mohan A, Singh AK, Kumar B, Dwivedi R. 2021. Review on remote sensing methods for landslide detection using machine and deep learning. Trans Emerg Telecommun Technol. 32(7): e3998. doi: 10.1002/ett.3998.

Monner D, Reggia JA. 2012. A generalized LSTM-like training algorithm for second-order recurrent neural networks. Neural Netw. 25(1):70–83. doi: 10.1016/j.neunet.2011.07.003.

Mora O, Mallorqui JJ, Broquetas A. 2003. Linear and nonlinear terrain deformation maps from a reduced set of interferometric SAR images. IEEE Trans Geosci Remote Sensing. 41(10):2243–2253. doi: 10.1109/TGRS.2003.814657.

Mu X, Wang S, Jiang P, Wang B, Wu Y, Zhu L. 2023. Full-coverage spatiotemporal estimation of surface ozone over China based on a high-efficiency deep learning model. Int J Appl Earth Obs Geoinformation. 118:103284. doi: 10.1016/j.jag.2023.103284.

Mullissa AG, Tolpekin V, Stein A, Perissin D. 2017. Polarimetric differential SAR interferometry in an arid natural environment. Int J Appl Earth Obs Geoinformation. 59:9–18. doi: 10.1016/j.jag.2017.02.019.

Nunziata F, Buono A, Migliaccio M, Benassai G. 2016. Dual-polarimetric C- and X-band SAR data for coastline extraction. IEEE J Sel Top Appl Earth Observations Remote Sensing. 9(11):4921–4928. doi: 10.1109/JSTARS.2016.2560342.

Otake R, Kurima J, Goto H, Sawada S. 2020. Deep learning model for spatial interpolation of real-time seismic intensity. Seismol Res Lett. 91(6):3433–3443. doi: 10.1785/0220200006.

Peng L, Liao X, Chen M. 2021. Resampling parameter estimation via dual-filtering based convolutional neural network. Multimed Syst. 27(3):363–370. doi: 10.1007/s00530-020-00697-y.

Pepe A, Solaro G, Calo F, Dema C. 2016. A minimum acceleration approach for the retrieval of multiplatform InSAR deformation time series. IEEE J Sel Top Appl Earth Observations Remote Sensing. 9(8):3883–3898. doi: 10.1109/JSTARS.2016.2577878.

Pu C, Xu Q, Wang X, Li Z, Chen W, Zhao K, Xiu D, Liu J. 2023. Refined mapping and kinematic trend assessment of potential landslides associated with large-scale land creation projects with multitemporal InSAR. Int J Appl Earth Obs Geoinformation. 118:103266. doi: 10.1016/j.jag.2023.103266.

Rianna G, Comegna L, Reder A, Urciuoli G, Picarelli L. 2023. A simplified procedure to assess the effects of climate change on landslide hazard in a small area of the Southern Apennines in Italy. Nat Hazards. 115(3):2633–2654. doi: 10.1007/s11069-022-05656-6.

Rivas-Medina A, Benito B, Gaspar-Escribano JM. 2018. Approach for combining fault and area sources in seismic hazard assessment: application in south-eastern Spain. Nat Hazards Earth Syst Sci. 18(11):2809–2823. doi: 10.5194/nhess-18-2809-2018.

Rosen PA, Gurrola EM, Sacco G, Zebker HA. 2011. InSAR Scientific Computing Environment - The Home Stretch. 2011: IN42A-02.

Samsonov S, d'Oreye N. 2012. Multidimensional time-series analysis of ground deformation from multiple InSAR data sets applied to Virunga Volcanic Province. Geophys J Int. 191(3): 1095–1108. doi: 10.1111/j.1365-246X.2012.05669.x.

Sellers C, Rodas R, Carrasco NP, De Stefano R, Di Martire D, Ramondini M. 2021. Ground deformation monitoring of a strategic building affected by slow-moving landslide in Cuenca (Ecuador). In: Rizzo P, Milazzo A, editors. Eur Workshop Struct Health Monit. Cham: Springer International Publishing; p. 149–158. doi: 10.1007/978-3-030-64908-1_14.

Shi X, Wang J, Jiang M, Zhang S, Wu Y, Zhong Y. 2022. Extreme rainfall-related accelerations in landslides in Danba County, Sichuan Province, as detected by InSAR. Int J Appl Earth Obs Geoinformation. 115:103109. doi: 10.1016/j.jag.2022.103109.

Solari L, Bianchini S, Franceschini R, Barra A, Monserrat O, Thuegaz P, Bertolo D, Crosetto M, Catani F. 2020. Satellite interferometric data for landslide intensity evaluation in mountainous regions. Int J Appl Earth Obs Geoinformation. 87:102028. doi: 10.1016/j.jag.2019.102028.

Sonnessa A, di Lernia A, Oscar Nitti D, Nutricato R, Tarantino E, Cotecchia F. 2023. Integration of multi-sensor MTInSAR and ground-based geomatic data for the analysis of non-linear displacements affecting the urban area of Chieuti, Italy. Int J Appl Earth Obs Geoinformation. 117:103194. doi: 10.1016/j.jag.2023.103194.

Sun Q, Hu J, Zhang L, Ding X. 2016. Towards slow-moving landslide monitoring by integrating multi-sensor InSAR time series datasets: the Zhouqu Case Study, China. Remote Sens. 8(11):908. doi: 10.3390/rs8110908.

Suzuki K, Ikehara M. 2020. Residual learning of video frame interpolation using convolutional LSTM. IEEE Access. 8:134185–134193. doi: 10.1109/ACCESS.2020.3010846.

Tasan M, Voosoghi B, Haji-Aghajany S, Amin Khalili M, Di Martire D. 2024. InSAR and GNSS data fusion for improved urban heat island estimation using local climate zone classification. Int J Appl Earth Obs Geoinformation. 130:103906. doi: 10.1016/j.jag.2024.103906.

Tings B, Jacobsen S, Wiehle S, Schwarz E, Daedelow H. 2021. X-Band/C-Band-Comparison of Ship Wake Detectability. In: EUSAR 2021 13th Eur Conf Synth Aperture Radar; p. 1–5.

Yunjun Z, Fattahi H, Amelung F. 2019. Small baseline InSAR time series analysis: unwrapping error correction and noise reduction. Comput Geosci. 133:104331. doi: 10.1016/j.cageo.2019.104331.

Zhang R, Zhu F, Liu J, Liu G. 2020. Depth-wise separable convolutions and multi-level pooling for an efficient spatial CNN-based steganalysis. IEEE TransInformForensic Secur. 15:1138–1150. doi: 10.1109/TIFS.2019.2936913.

Zhao C, Lu Z. 2018. Remote sensing of landslides: a review. Remote Sens. 10(2):279. doi: 10.3390/rs10020279.

Zhao Z, Chen J, Xu K, Xie H, Gan X, Xu H. 2021. A spatial case-based reasoning method for regional landslide risk assessment. Int J Appl Earth Obs Geoinformation. 102:102381. doi: 10.1016/j.jag.2021.102381.